The Cryosphere Discuss., 9, 6061–6123, 2015
www.the-cryosphere-discuss.net/9/6061/2015/
doi:10.5194/tcd-9-6061-2015

The Cryosphere Discussions
Open Access
EGU

Anisotropy of seasonal snow measured by polarimetric phase differences in radar time series

S. Leinss[1], H. Löwe[2], M. Proksch[2], J. Lemmetyinen[3], A. Wiesmann[4], and I. Hajnsek[1,5]

[1]Institute of Environmental Engineering, Swiss Federal Institute of Technology (ETH), Zürich, Switzerland
[2]Institute for Snow and Avalanche Research SLF, Davos, Switzerland
[3]Finnish Meteorological Institute FMI, Arctic Research, Sodankylä, Finland
[4]GAMMA Remote Sensing AG, Gümlingen, Switzerland
[5]Microwaves and Radar Institute, German Aerospace Center (DLR), Wessling, Germany

Received: 1 October 2015 – Accepted: 9 October 2015 – Published: 5 November 2015

Correspondence to: S. Leinss (leinss@ifu.baug.ethz.ch)

Published by Copernicus Publications on behalf of the European Geosciences Union.

Abstract

Snow settles under the force of gravity and recrystallizes by vertical temperature gradients. Both effects are assumed to form oriented ice crystals which induce an anisotropy in mechanical, thermal, and dielectric properties of the snow pack. On microscopic scales, the anisotropy could be hitherto determined only from stereology or computer tomography of samples taken from snow pits. In this paper we present an alternative method and show how the anisotropy of a natural snow pack can be observed contact- and destruction-free with polarimetric radar measurements. The copolar phase differences (CPD) of polarized microwaves transmitted through dry snow were analyzed for four winter seasons (2009–2013) from the SnowScat Instrument, installed at a test site near the town of Sodankylä, Finnland. An electrodynamic model was established based on anisotropic optics and on Maxwell–Garnett-type mixing formulas to provide a link between the structural anisotropy and the measured CPD. The anisotropy values derived from the CPD were compared with in-situ anisotropy measurements obtained by computer tomography. In addition, we show that the CPD measurements obtained from SnowScat show the same temporal evolution as space-borne CPD measurements from the satellite TerraSAR-X. The presented dataset provides a valuable basis for the future development of snow models capable of including the anisotropic structure of snow.

1 Introduction

Deposited snow is a porous and highly metamorphic material which continuously undergoes recrystallization processes to adapt to the external thermodynamic forcing determined by the atmosphere and the underlying soil. The microstructure of the sintered snow crystals constitutes thermal, mechanical and electromagnetic properties of snow. Hence, an anisotropic microstructure leads to a macroscopic anisotropy of snow properties. Characterization of the microstructure is difficult and requires work inten-

TCD
9, 6061–6123, 2015

sive sampling which can disturb the natural snow structure irreversibly by snow pits, sieving, sample-taking or cutting of samples.

Before the introduction of micro computer-tomography (μCT), microscopic data about the snow structure was rare. The only method providing microscopic information was stereology, which is based on cutting snow into thin sections. Nevertheless, vertical structures have been identified in thin sections of polar snow (Alley, 1987). Furthermore, formation of anisotropic, vertical snow structures has been observed by thin section photography, when snow recrystallization was driven by a vertical water vapor flux (Pfeffer and Mrugala, 2002). Vertical structures have also been found in conjunction with anisotropic thermal conductivities (Izumi and Huzioka, 1975). Also horizontal structures have been identified using stereology in fresh snow (Davis and Dozier, 1989), (Mätzler, 1987, Fig. 2.15, left[1]).

The anisotropy of snow can statistically be determined from the heterogeneous snow matrix by spatial correlation functions (Vallese and Kong, 1981; Mätzler, 1997) of stereological (Alley, 1987; Mätzler, 2002) or computer tomography data (Löwe et al., 2011, 2013). Today, computer tomography is the "state of the art" for destruction-free observation of the snow microstructure within volumes of a few cm^3 and with a spatial resolution of a few micrometers. Even a temporal resolution is possible for snow samples which are kept under laboratory conditions (Schneebeli and Sokratov, 2004). Laboratory experiments revealed the characteristics of grain growth and sintering during isothermal metamorphism (Kaempfer and Schneebeli, 2007) as well as during alternating temperature gradients which occur on daily cycles (Pinzer and Schneebeli, 2009). Anisotropic structures have been identified and the recrystallization process was observed where initially horizontally oriented ice grains recrystallized to vertical structures during exposure to a vertical temperature gradient (Schneebeli and Sokratov, 2004; Riche et al., 2013; Calonne et al., 2014). Vertical structures have also been found in samples of polar firn (Hörhold et al., 2009; Lomonaco et al., 2011) and vertical and

[1]Note that the captions of Figs. 2.15 and 2.14 in (Mätzler, 1987) have been inadvertently swapped.

TCD
9, 6061–6123, 2015

horizontal structures have been found in seasonal snow (Calonne et al., 2012). The origin of horizontally aligned structures has been discussed with respect to settling of fresh snow (Schleef and Löwe, 2013). Settling is also assumed to be the reason for horizontal anisotropies which were found in the intermediate stage of isothermal metamorphism, since for isothermal conditions only gravity breaks the symmetry between vertical and horizontal directions (Löwe et al., 2011).

On macroscopic scales, the anisotropy of snow can be determined by measuring the anisotropy of the dielectric permittivity. Despite the fact that the dielectric anisotropy is much smaller than the anisotropy of the thermal conductivity (Löwe et al., 2013), the dielectric anisotropy can be measured with different polarizations of the electromagnetic field in microwave resonators filled with snow (Jones, 1976). Using open microwave resonators, different permittivities in the vertical and horizontal direction have been found in multi-year firn on the Greenland ice sheet (Fujita et al., 2014). Anisotropy measurements with microwave resonators were also performed in conjunction with photographic (Lytle and Jezek, 1994) and computer tomographic analysis (Fujita et al., 2009). It is even possible to determine the anisotropy of seasonal snow with radar satellites, when propagation differences of differently polarized microwaves are analyzed (Leinss et al., 2014). Also with passive microwave sensors, strong polarimetric signatures have been found over the Greenland ice sheet: in (Li et al., 2008), the found passive microwave signatures could not be explained by surface features, but were discussed with respect to microstructural variations of the anisotropy of snow, as predicted by Tsang (1991).

Polarimetric radar remote sensing methods provide a contactless tool to measure the anisotropy of snow destruction-free, and from large distances. Areas of many thousands of km^2 can be observed with air- and space-borne sensors. They provide a complementary tool to computer tomography as large areas and volumes of natural snow can be observed. Still, publications related to polarimetric propagation effects in deposited snow are rare, despite the fact that a differential propagation speed in falling snow was already noticed in 1976 for weather radars (Hendry et al., 1976). Cur-

TCD
9, 6061–6123, 2015

rently, polarimetric radars are only used to characterize the anisotropy of falling snow or rain (Garrett et al., 2012; Xie et al., 2012; Hogan et al., 2012; Noel and Chepfer, 2010; Tyynelä and Chandrasekar, 2014). However, in 1992, microwave experiments in Greenland revealed a directional propagation speed in firn (Lytle and Jezek, 1994), caused by a vertical anisotropy. In 1996, the opposite effect was observed, when the phase difference between vertically (VV) and horizontally (HH) polarized microwaves, the so called Copolar Phase Difference, CPD, measured by a ground-based radar increased after snow fall. The increase of the CPD was explained by a horizontal anisotropy of deposited fresh snow (Chang et al., 1996). Both effects were observed in satellite time series of TerraSAR-X, where a significant positive correlation between the CPD and the depth of fresh snow was found, but also the opposite effect was observed, where a strong temperature gradient in the snow pack forced the CPD towards negative values (Leinss et al., 2014).

The CPD is a very sensitive observable to measure dielectric anisotropies because relative signal delays much smaller than the ratio between the radar wavelength and the snow depth can be measured. This interferometric approach makes it possible to determine dielectric anisotropies with a precision down to $\Delta\epsilon \approx 10^{-4}$.

In this paper, we present an electromagnetic model to determine the mean anisotropy of a dry snow pack from the CPD measured by polarimetric radar systems. The model consistently builds on the description of the microstructure of snow in terms of spatial correlation functions. The model is applied on CPD measurements acquired with the SnowScat Instrument (Wiesmann et al., 2008; Werner et al., 2010) within four winter seasons from 2009 to 2013. The CPD time series are discussed with respect to snow fall, snow metamorphism and melting. For three selected dates, we compare the derived anisotropy with the anisotropy determined by computer-tomography. Furthermore, we compare the measured time series of two winter seasons with space-borne observations from TerraSAR-X and TanDEM-X and discuss the question, of whether the CPD can be used to determine the depth of fresh snow.

TCD
9, 6061–6123, 2015

2 Electromagnetic model for measuring the anisotropy with polarimetric radar systems

In this section we provide a relation between the structural anisotropy of snow, the effective dielectric permittivity ε_{eff}, and the Copolar Phase Difference (CPD) measured by a polarimetric, side-looking radar system.

2.1 Definition of structural anisotropy

We define the structural anisotropy, A, as the normalized difference between the characteristic horizontal dimension, a_x, and the characteristic vertical dimension, a_z, of the "grains" in the ice matrix:

$$A = \frac{a_x - a_z}{\frac{1}{2}(a_x + a_z)} \tag{1}$$

Different choices for the length scales a_x and a_z are possible. Recent work has mainly used the (exponential) correlation lengths, $a_x = p_{\text{ex},x}$ and $a_z = p_{\text{ex},z}$, as defined in Mätzler (2002) and derived from spatial correlation functions (Löwe et al., 2011).

If the anisotropy is defined as in Eq. (1), the magnitude of A for grains with given ratio between longest and shortest length is independent of whether the longest length is vertically or horizontally oriented. This is different for an alternative definition A' where the anisotropy is defined as the vertical-to-horizontal size ratio of ice grains. The definition A' is commonly used to simplify electromagnetic modeling. The anisotropy A' can be converted to Eq. (1) by

$$A' = \frac{a_z}{a_x} = \frac{2 - A}{2 + A} \quad \text{or} \quad A = \frac{1 - A'}{\frac{1}{2}[1 + A']}. \tag{2}$$

We note that the anisotropy A' differs from the definition in terms of the "degree of anisotropy" (DA) which is used in (Hildebrand et al., 1999; Schneebeli and Sokratov,

TCD
9, 6061–6123, 2015

2004). For the DA, the absolute orientation in space is lost since the definition is based on the ratio of the largest and smallest eigenvalues of the mean intersection length (MIL) tensor. The anisotropy A' (defined as ϵ in Torquato and Lado, 1991 or $\mathcal{A}(l_c)$ in Calonne et al., 2014) can be further related to the anisotropy-parameter Q used in Calonne et al. (2014) by the definition in Löwe et al. (2013, Eq. 4).

In the following we define the coordinate axes such that z is parallel to the normal vector of the earth surface and the x and y plane is parallel to the flat earth surface. We restrict our model to flat terrain and do not consider shear stress or temperature gradients not parallel to gravity, which can both occur on steep terrain.

2.2 Relative permittivity as a function of anisotropic inclusions

The CPD measured by polarimetric radar systems depends on the difference of the dielectric permittivity ε_{eff} measured in the x and z direction. The aim of this subsection is to establish a link between the effective permittivity $\varepsilon_{\text{eff},i}$ for $i \in \{x, y, z\}$ and the structural anisotropy A.

The following model is based on an empirical extension of the classical Maxwell–Garnett mixing formulas for aligned mixtures of ice inclusions in a host medium of air (e.g. Polder and van Santen, 1946; Sihvola, 2000). To motivate the necessity of the empirical extension we briefly revisit the application of Maxwell–Garnett mixing formulas in the isotropic case. For isotropic snow ($A = 0$) the permittivity $\varepsilon_{\text{eff},i}$ should agree with measurements of ε for isotropic snow. However, the relative permittivity, $\varepsilon_{\text{eff, MG}}$, calculated with the Maxwell–Garnett formula underestimates the measured permittivity (Mätzler, 1996). It was found that $\varepsilon_{\text{eff, MG}}$ is equivalent with the lower Hashin–Shtrikman bound (Sihvola, 2002; Hashin and Shtrikman, 1962). The upper Hashin–Shtrikman bound is equivalent with the "inverse" Maxwell–Garnett formula, $\varepsilon_{\text{eff, MG, inv}}$, which models air inclusions in a host medium of ice (Sihvola, 2002). Therefore it is preferable to combine both bounds in a reasonable way to determine ε_{eff}. We found that the fol-

TCD
9, 6061–6123, 2015

lowing weighted average agrees with (Wiesmann and Mätzler, 1999, Eqs. 45 and 46)[2] within less than ±0.7 %

$$\varepsilon_{\text{eff}} = \left(\varepsilon_{\text{eff, MG}} + \varepsilon_{\text{eff, MG, inv}} \cdot f_{\text{vol}} \varepsilon_{\text{ice}}\right) / (1 + f_{\text{vol}} \varepsilon_{\text{ice}}). \quad (3)$$

The ice volume fraction f_{vol} relates the density of snow ρ to the volumetric mass density of air and ice by

$$\rho = f_{\text{vol}} \cdot \rho_{\text{ice}} + (1 - f_{\text{vol}}) \cdot \rho_{\text{air}} \approx f_{\text{vol}} \cdot \rho_{\text{ice}}. \quad (4)$$

In the microwave regime, the relative permittivity of pure ice is given by $\varepsilon_{\text{ice}} = 3.17 \pm 0.02$, and shows a weak temperature dependence (Mätzler and Wegmüller, 1987; Fujita et al., 1993; Warren and Brandt, 2008; Bohleber et al., 2012). According to the Maxwell–Garnett theory for isotropic mixtures, $\varepsilon_{\text{eff, MG}}$ is given by

$$\varepsilon_{\text{eff, MG}} = \varepsilon_{\text{air}} + 3 f_{\text{vol}} \varepsilon_{\text{air}} \frac{\varepsilon_{\text{ice}} - \varepsilon_{\text{air}}}{\varepsilon_{\text{ice}} + 2\varepsilon_{\text{air}} - f_{\text{vol}}(\varepsilon_{\text{ice}} - \varepsilon_{\text{air}})} \quad (5)$$

with the relative permittivity of air, $\varepsilon_{\text{air}} = 1$ (e.g. Sihvola, 2000). The "inverse" Maxwell–Garnett result, $\varepsilon_{\text{eff, MG, inv}}$, follows by swapping ε_{air} and ε_{ice} in Eq. (5) and replacing f_{vol} by $1 - f_{\text{vol}}$ (Sihvola, 2002). Note that the Maxwell–Garnett theory is a mean-field theory and additionally requires the inclusions to be much smaller than the wavelength of the microwaves in the medium ($a_x, a_y, a_z \ll \lambda / \sqrt{\varepsilon_{\text{eff}}}$), so that scattering in the snow volume can be neglected.

For non-spherical inclusions, Eq. (5) has to be adapted by introducing depolarization factors, N_i, for aligned ellipsoidal inclusions (e.g. Cohn, 1900; Polder and van Santen, 1946, or Sihvola, 2000). As settling and temperature gradient metamorphism act in the z direction, we model the elliptical inclusions as oblate or prolate spheroids which

[2] Eq. (46) in Wiesmann and Mätzler (1999) has been adapted to produce correct results for pure ice ($\nu = 1$). The adapted factors are $\varepsilon_h = 1.005$ and $\varepsilon_s = 3.17^{1/3}$.

TCD
9, 6061–6123, 2015

have their symmetry axis parallel to z. According to (Sihvola, 2000) the permittivity of anisotropic mixtures is given for each spatial dimension $i \in x, y, z$ by

$$\varepsilon_{\text{eff, MG},i} = \varepsilon_{\text{air}} + f_{\text{vol}}\varepsilon_{\text{air}} \frac{\varepsilon_{\text{ice}} - \varepsilon_{\text{air}}}{\varepsilon_{\text{air}} + (1 - f_{\text{vol}})N_i(\varepsilon_{\text{ice}} - \varepsilon_{\text{air}})} \tag{6a}$$

The "inverse" Maxwell–Garnett form of Eq. (6a) reads

$$\varepsilon_{\text{eff, MG, inv},i} = \varepsilon_{\text{ice}} + (1 - f_{\text{vol}})\varepsilon_{\text{ice}} \frac{\varepsilon_{\text{air}} - \varepsilon_{\text{ice}}}{\varepsilon_{\text{ice}} + f_{\text{vol}}N_i(\varepsilon_{\text{air}} - \varepsilon_{\text{ice}})}. \tag{6b}$$

Both equations are used in Eq. (3) to calculate the effective anisotropic relative permittivities $\varepsilon_{\text{eff},x}, \varepsilon_{\text{eff},y}$ and $\varepsilon_{\text{eff},z}$ for snow. Results for the permittivity and the deviation from the isotropic case are shown in Fig. 1.

The depolarization factors N_i are assumed to be equivalent for both Eqs. (6a) and (6b) and are given according to (Sihvola, 2000) for ellipsoidal inclusions with the dimensions a_x, a_y, a_z by

$$N_i = \frac{a_x a_y a_z}{2} \int_0^\infty \frac{\mathrm{d}s}{(s + a_i^2)\sqrt{(s + a_x^2)(s + a_y^2)(s + a_z^2)}}. \tag{7}$$

The dimensions $a_x = a_y$ define the diameter of the spheroids and a_z is their vertical length. Note that Sihvola (2000) used the ellipsoids' semi-axis. However, the depolarization factors do not depend on the absolute size of inclusions and are invariant under rescaling $a_i \to \lambda a_i$ for arbitrary λ. Consequently, it is possible to parametrize the depolarization factors directly by the anisotropy A', which can easily be verified by substituting s in Eq. (7) with the dimensionless quantity $u = s/a_x^2$. N_i is then given by

$$N_i = \frac{A'}{2} \int_0^\infty \frac{\mathrm{d}u}{(u + \delta_{A'}(i,z))\sqrt{(u+1)^2 \cdot (u + A'^2)}} \tag{8}$$

TCD
9, 6061–6123, 2015

with $\delta_{A'}(i,z) = 1$ for $i \in x,y$ and $\delta_{A'}(i,z) = A'^2$ for $i = z$. Closed form expressions for the elliptic integrals can be found e.g. in Sihvola (2000). The depolarization factors satisfy $N_x + N_y + N_z = 1$ for any ellipsoid (Polder and van Santen, 1946). For spherical inclusions all three depolarization factors are $N_i = 1/3$ and Eq. (6a) is equivalent with Eq. (5).

Although ice grains show a much more complex structure than simple ellipsoids, the model of ellipsoids is realistic enough for the transverse isotropic symmetry of the dielectric tensor $\overline{\overline{\varepsilon}}$. This becomes more obvious from the exact series expansion of the dielectric tensor for arbitrary anisotropic microstructures, which can be expressed in terms of spatial correlation functions (Rechtsman and Torquato, 2008). In the Appendix, we show that under the less restrictive assumption of a transverse isotropic two-point correlation function, the truncation of the exact expression using n-point correlation functions (Rechtsman and Torquato, 2008, Eq. 16) at second order ($n = 2$) *exactly* leads to the Maxwell–Garnett result (Eq. 6a) in which the depolarization factors N_i are expressed in terms of the anisotropy parameter Q as given in (Löwe et al., 2013) via $N_i = Q$ for $i = x,y$ and $N_z = 1 - 2Q$. This implies that the present dielectric model and the thermal conductivity model from (Löwe et al., 2013) are based on exactly the same microstructural parameters. In view of recent attempts to unify microstructural descriptions of snow for microwave modeling (Löwe and Picard, 2015), we also note that the Maxwell–Garnett formula (Eq. 6a) can be likewise obtained as the low-frequency limit of the quasi-crystalline approximation for aligned spheroids (Ao and Kong, 2002).

2.3 Anisotropy measured by radar systems

In the previous section, the anisotropic effective permittivity $\varepsilon_{\mathrm{eff},i}$ was derived for snow which has a spatially anisotropic microstructure. The effective permittivity can be measured when snow is observed with a polarimetric radar system by analyzing the Copolar Phase Difference, CPD. The CPD is a measure for the propagation delay of orthogonally polarized microwaves and is derived in this section with respect to $\varepsilon_{\mathrm{eff},i}$.

TCD
9, 6061–6123, 2015

Only side-looking polarimetric radar systems like real or synthetic aperture radar systems are suitable for measuring the anisotropy of snow, whereas nadir-looking radar systems like ground penetrating radars are not. A requirement to measure the anisotropy is that the two orthogonal polarized microwaves are delayed by different components of the dielectric tensor $\overline{\overline{\varepsilon}}$. The sensitivity to the anisotropy increases linearly with frequency. However, the radar system must operate at a low enough frequency (several GHz) such that microwaves can penetrate dry snow with negligible scattering or absorption losses (e.g. Hallikainen et al., 1987; West et al., 1993; Tsang et al., 2007, or Leinss et al., 2015, Fig. 5).

The dielectric anisotropy can precisely be measured with the CPD, because the CPD can be determined with a precision of a few degrees (fraction of one wavelength) relative to the total phase delay of many wavelengths which is accumulated during propagation through the snow pack (Guneriussen et al., 2001, Eq. 5), and (Leinss et al., 2015, Eq. 14). For example, for 1 m deep snow of density $\rho = 0.25\,\mathrm{g\,cm^{-3}}$ a dielectric anisotropy $\epsilon_x - \epsilon_z = 10^{-4}$ causes a CPD of 1° relative to the total phase delay of 5700° measured at a radar frequency of 10 GHz and a radar incidence angle of 40°.

In order to derive the CPD, the wave propagation through snow is formulated analogue to transversely isotropic media as done in anisotropic optics (Saleh and Teich, 1991). Considering snow as transversely isotropic is reasonable since gravity and the direction of the water vapor flux in snow break isotropy in the vertical direction, therefore the optical axis is given by the z axis.

According to anisotropic optics, we define the refractive index in the z direction as the extraordinary refractive index n_e. For transversely isotropic media, the extraordinary refractive index, n_e, differs from the ordinary refractive indices, n_o, which is defined in the (x, y) plane (Fig. 2). The refractive indices are related to the relative permittivity defined in Eq. (3) together with Eqs. (6a) and (6b) by

$$n_\mathrm{o}^2 = \varepsilon_{\mathrm{eff},x} = \varepsilon_{\mathrm{eff},y} \tag{9a}$$

$$n_\mathrm{e}^2 = \varepsilon_{\mathrm{eff},z}. \tag{9b}$$

TCD
9, 6061–6123, 2015

The anisotropy of snow can only be determined with polarimetric radar systems when microwaves are transmitted with a large enough incidence angle θ_0 with respect to the optical axis. The polarizations of a side-looking radar system are defined orthogonal to the propagation vector $\boldsymbol{k}$ of the incident beam such that the horizontal polarization (H) is oriented parallel to the observed surface (cf. Fig. 2). Hence, the H-polarization is delayed by the ordinary refractive index n_0. The vertical polarization (V) is defined perpendicular to H and the propagation vector $\boldsymbol{k}$. The V-polarization is not parallel to the optical axis z as for side-looking radar systems the incidence angle θ_0 can never reach 90°. Therefore, the electric field of the V-polarization always has one component along the optical axis z and one component perpendicular to it, along x. For the V polarization, the refractive index n_V depends on the propagation angle θ_V in the medium and can be described by the refractive index ellipsoid (Saleh and Teich, 1991)

$$\frac{1}{n_V^2(\theta_V)} = \frac{\cos^2\theta_V}{n_o^2} + \frac{\sin^2\theta_V}{n_e^2}. \tag{10}$$

The refractive indices for the H and V polarized wave are[3]

$$n_H = n_o \tag{11a}$$

$$n_V(\theta_V) = \frac{n_o n_e}{\sqrt{n_e^2\cos^2\theta_V + n_o^2\sin^2\theta_V}}. \tag{11b}$$

The refraction at the air-snow interface is described by Snell's law which for the H polarization is

$$n_{air}\sin\theta_0 = n_H\sin\theta_H. \tag{12a}$$

[3]Note that the equation for n_V^2 in (Leinss et al., 2014) is an approximation of Eq. (10) for small anisotropies. The approximation follows from Eq. (10) by writing $n_o^2 = \epsilon_{eff} - \delta$ and $n_i^2 = \epsilon_{eff} + \delta$ and applying a first order Taylor expansion in δ, neglecting terms $\mathcal{O}(\delta^2/\epsilon^2)$.

TCD
9, 6061–6123, 2015

For the V polarization, the refractive index n_V depends on θ_V, which in turn depends on n_V. The modified Snell's law

$$n_{air} \sin\theta_0 = n_V(\theta_V) \sin\theta_V \tag{12b}$$

has therefore to be solved simultaneously with Eq. (11b). It follows that

$$n_V(\theta_V) = \sqrt{n_o^2 + \left(1 - \frac{n_o^2}{n_e^2}\right) n_{air}^2 \sin^2\theta_0}. \tag{13}$$

Equation (13) can be used in Eq. (12b) to calculate the angle θ_V. Note, that θ_V is only implicitly contained in Eq. (13) by θ_0 and Snell's law (12b). For a birefringent medium, θ_V does no longer describe the direction of propagation of an optical beam (which does the Poynting-Vector), but instead the direction which is perpendicular to the wave fronts (the wave vector $\boldsymbol{k}$). As we are interested in the retardation of wave fronts, we use θ_V which determines the direction of $\boldsymbol{k}$ in the birefringent medium. For multi-layer systems comprising N anisotropic layers which all have the optical axis parallel to the z axis, Eqs. (12a) and (12b) are valid for every layer because Snell's law holds at each layer-interface

$$n_j \sin\theta_j = n_{j+1} \sin\theta_{j+1} \text{ for } j = 0, 1 \ldots N-1 \tag{14}$$

and with $n_0 = n_{air}$. The difference in propagation delay between both polarizations can now be calculated. Fig. 2 shows the geometry of a multilayer system where each layer j can have a different anisotropy A_j and density ρ_j. The layers are numbered from top (1) to bottom (N). Two sinusoidal plane waves, described by $\boldsymbol{E}(t, \boldsymbol{r}) = \boldsymbol{E}_0 e^{i(\omega t - \boldsymbol{k}\boldsymbol{r})}$ with the same frequency $\nu = \omega/(2\pi)$ are transmitted to the snow surface with an incidence angle θ_0. For a fixed time t, the phase difference measured along a distance r is given by $\phi = \boldsymbol{k} \cdot \boldsymbol{r}$, where the magnitude of the wave vector $|\boldsymbol{k}| = \frac{2\pi n}{\lambda_0}$ in the medium is defined by the refractive index n and the vacuum wavelength λ_0. The two paths for the ordinary

TCD
9, 6061–6123, 2015

(H) and extraordinary (V) waves which connect a common wave front with a point P at the snow-soil interface are shown in Fig. 2. The two-way phase difference along this path is given by

$$\phi_{\mathrm{CPD}} = \phi_{\mathrm{VV}} - \phi_{\mathrm{HH}} \tag{15}$$

which correspond to the measured copolar phase difference (CPD) between the VV and HH channel of a radar system. The two letters corresponds to the polarization of the transmitting (V and H) and receiving (V and H) channel. For monostatic radar systems, the same coordinate system (H, k, V) is used for transmission and reception of the microwave signal, which is called "Back-Scatter Alignment" convention, BSA. The reversal of the $\boldsymbol{k}$ vector in the BSA causes a sign-change of the phase ϕ, hence the physically expected phase difference ϕ'_{CPD} is related to the phase difference measured in the BSA coordinate system by $\phi_{\mathrm{CPD}} = (-1)\phi'_{\mathrm{CPD}}$ (cf. Lüneburg and Boerner, 2004 or Lee et al., 1999, Sect. 3.1.3). With respect to Fig. 2, the polarimetric propagation delay and consequently the CPD is given by the phase accumulated during the propagation through the snow pack plus an offset in air

$$\begin{aligned}\phi'_{\mathrm{CPD}} &= 2\sum_{j=1}^{N}\Delta\phi_{\mathrm{V},j} - 2\sum_{j=1}^{N}\Delta\phi_{\mathrm{H},j} - 2\phi_{\mathrm{air}} \\ &= 2\sum_{j=1}^{N}\frac{k_{\mathrm{V},j}\Delta z_j}{\cos\theta_{\mathrm{V},j}} - 2\sum_{j=1}^{N}\frac{k_{\mathrm{H},j}\Delta z_j}{\cos\theta_{\mathrm{H},j}} - 2\phi_{\mathrm{air}}.\end{aligned} \tag{16}$$

The in-air phase difference $\phi_{\mathrm{air}} = k_0\Delta L_{\mathrm{air}}$ depends on the sum of horizontal displacements $\sum\Delta x_{\mathrm{V},j} - \Delta x_{\mathrm{H},j}$ and is given by

$$\phi_{\mathrm{air}} = k_0 \cdot \sin\theta_0 \sum_{j=1}^{N}\Delta z_j\left(\tan\theta_{\mathrm{V},j} - \tan\theta_{\mathrm{H},j}\right). \tag{17}$$

TCD
9, 6061–6123, 2015

The ordinary and extraordinary wave vectors are given by

$$k_{\mathrm{H}} = \frac{2\pi n_{\mathrm{H}}}{\lambda_0} \quad \text{and} \quad k_{\mathrm{V}} = \frac{2\pi n_{\mathrm{V}}}{\lambda_0}. \tag{18}$$

Equation (16) can be rearranged and combined with Eqs. (17) and (18) and it follows that the CPD can be formulated in the BSA convention by

$$\phi_{\mathrm{CPD}} = (-1)\frac{4\pi}{\lambda_0}\sum_{j=1}^{N}\Delta z_j \cdot \Delta\zeta(\rho_j, A_j, \theta_0). \tag{19}$$

The contributions of individual layers of thickness Δz are given by the relative path length difference

$$\Delta\zeta(\rho, A, \theta_0) = \sqrt{n_{\mathrm{V}}^2 - \sin^2\theta_0} - \sqrt{n_{\mathrm{H}}^2 - \sin^2\theta_0}. \tag{20}$$

The relative path length difference defines the optical path length difference relative to the thickness ΔZ of an anisotropic medium observed under a surface incidence angle θ_0. The refractive indices n_{V} and n_{H} are defined for each individual layer by Eqs. (11a) and (13) using the effective permittivity from Eqs. (9a) and (9a), which was derived in Sect. 2.2 for snow density ρ and anisotropy A.

The horizontal structures in settled fresh snow causes a faster propagation speed for the VV polarization than for HH. Consequently, HH will have a larger phase delay than VV at the receiving antenna. This results in a positive(!) copolar phase difference $\phi_{\mathrm{VV}} - \phi_{\mathrm{HH}}$, due to a sign-change because of the BSA.

The relative path length difference, $\Delta\zeta$, increases with incidence angle (Fig. 3, left) and with increasing densities below $0.2\,\mathrm{g\,cm^{-3}}$ (Fig. 3, right). When the snow density increases beyond $0.3\,\mathrm{g\,cm^{-3}}$, refraction reduces the alignment of the V polarization with respect to the optical axis and consequently $\Delta\zeta$ decreases (Fig. 3, right). Also, above a density of about $\rho = 0.55$, the dielectric contrast $\varepsilon_x - \varepsilon_z$ decreases (Fig. 1,

TCD
9, 6061–6123, 2015

right) such that $\Delta\zeta$ vanishes at $\rho = \rho_{ice}$ where no air inclusions are present anymore. A broad maximum of $\Delta\zeta$ is observed for densities between 0.2 and 0.4 g cm^{-3} (Fig. 3, right), where almost no density dependence exists.

In contrast to the non-invertible density dependence of $\Delta\zeta$, $\Delta\zeta$ depends almost linearly on anisotropy A for all densities and incidence angles (Fig. 4, left and right).

When we use Eq. (19) to calculate the CPD, we get about 5–10 % lower values compared to the theory in Leinss et al. (2014) where refraction was not included. Refraction leads to a decreasing z component of the V polarization, consequently the birefringent effect is reduced as well. Using the weighted average of the two Hashin–Shtrikman bounds to calculate ε_{eff} leads to an additional decrease of up to 30 % for higher snow densities.

For firn with $\rho = 0.4\,\mathrm{g\,cm^{-3}}$, $\Delta\varepsilon = +0.05$, as observed in Fujita et al. (2014), we would expect $\phi_{CPD} = 70^\circ$ per meter and a vertical anisotropy $A = -0.37$ ($A' = 1.4$). In Leinss et al. (2014) a CPD of 6–15°/10 cm of fresh snow was measured at 32.7° and 9.65 GHz, which would correspond to a horizontal anisotropy between $A = +0.2$ and $+0.5$ ($A'^{-1} = 1.2$ and 1.7). Similar anisotropy values have been observed in Alley (1987); Schneebeli and Sokratov (2004).

2.4 Generalization for scattering multilayer systems

Equation (19) is valid for a multi-layer system, where scattering and absorption are negligible in or between different snow layers. In the present work, we solely concentrate on non-scattering and non-absorptive media for which all scattered energy returns from the bottom of the multi-layer snow system.

For multi-layer systems like snow with very large ice grains, e.g. deep multi-year firn on glaciers, but also for wet and consequently absorbing snow, the location of the main scattering center is difficult to define and depends strongly on the scattering properties of the snow volume. In the following we briefly outline how Eq. (19) can be generalized when scattering of different layers needs to be included.

TCD
9, 6061–6123, 2015

In order to generalize our model for media where volume scattering cannot be neglected, we define – possibly complex – amplitude scattering factors μ_j for each layer boundary. The phasor $e^{i\phi_1}$ which results from the CPD of the first layer contributes with μ_j to the total phase difference. The reflection from the second layer accumulates the CPD of the first and of the second layer, so that the second phasor is given by $e^{i(\phi_1+\phi_2)}$ and so on. The total phase difference is then

$$\phi_{\mathrm{CPD}} = \mu_1 \cdot e^{i\phi_1} + \mu_2 \cdot e^{i(\phi_1+\phi_2)} + \ldots = \sum_{j=1}^{N} \mu_j \prod_{k=1}^{j} e^{i\phi_j}. \quad (21)$$

For homogeneously scattering and/or absorbing volumes, $|\mu_j|$ would decrease exponentially, whereas μ_j can be quite heterogeneous for ice layers which occur e.g. in the percolation zone of glaciers (Parrella et al., 2015). In such cases, assumptions must be made for the penetration depth or the penetration depth must be determined independently.

3 Experimental data

For the validation of our model we analyzed radar data acquired within the Nordic Snow Radar Experiment (NoSREx) campaigns (Lemmetyinen et al., 2013). The NoSREx campaigns consisted of extensive field measurements and various active and passive microwave measurements at a test site near the city Sodankylä in northern Finland. The test site, shown in Fig. 5, is an almost flat forest clearing which is surrounded by boreal forest. Low taiga-type vegetation grows on the site on mineral soil. During winter, the site was covered quite homogeneously with snow. The variability of snow depth showed a standard deviation of 2–3 cm and was measured with seven sticks located 1 m apart. The seven sticks are indicated by "SDvar" in Fig. 5.

TCD
9, 6061–6123, 2015

3.1 Microwave measurements

The radar data was acquired by the SnowScat Instrument (SSI), which was installed on a 9 m high tower on the test site. The SSI is shown in the inset of Fig. 5.

SnowScat is a fully polarimetric, coherent, continuous-wave stepped-frequency, real aperture radar and operates between 9.2 and 17.8 GHz (Wiesmann et al., 2008; Werner et al., 2010). It was originally developed and built for snow backscatter measurements within the ESA ESTEC project KuScat, contract No. 42000 20716/07/NL/EL. Both antennas of the instrument can transmit and receive in horizontal (H) and vertical (V) polarization.

The test site contained two sectors for which measurements were repeated every four hours. The sectors were scanned in azimuth-subsectors of 6° by rotating the antennas around the vertical axis (*az*). The scan was done for each of the four nominal incidence angles ($\theta_0 = 30^\circ, 40^\circ, 50^\circ$, and 60°) resulting in 17×4 acquisitions for sector 1 and 5×4 acquisitions for sector 2. Each subsector was measured in all four polarization combinations pol $\in \{VV, HH, VH, HV\}$. A detailed description showing the acquisition geometry, antenna patterns and the polarimetric backscatter signal from the two sectors can be found in (Leinss et al., 2015).

3.2 Meteorological measurements

Several instruments were installed at the test site which automatically measured meteorological data. Fig. 5 shows the location of different sensors. Snow depth and air temperature were measured by the sensor SDTA1. Soil temperature and soil moisture were measured by two sensors named SMT. An automatic weather station (AWS), located 500 m north of the SSI measured snow depth, air temperature, and other meteorological parameters.

TCD
9, 6061–6123, 2015

3.3 Snow measurements

Snow density was manually measured in the snow pit once every week. Snow density was also calculated from snow depth measured by SDTA1 and from SWE measurements. SWE was obtained from the SSI during dry snow conditions, and from measurements of the Gamma Water Instrument, GWI, during wet snow conditions. Details for SWE determination can be found in Leinss et al. (2015).

The microstructure of vertical snow profiles was determined at three sites, CT-1 on 21 December 2011, CT-2 on 1 March 2012, and CT-3 on 28 February 2013. The location of the sites are shown in Fig. 5. Overlapping samples where taken to cover entire snow depth profiles. The samples were later analyzed by computer tomography at the Institute for Snow and Avalanche Research SLF in Switzerland. For analysis by means of μCT, the snow samples had to be cast for transportation from Finland to the cold lab at SLF, Switzerland.

An analysis of the μCT data, which we used here to determine the anisotropy, was already published with respect to other snow structure parameters in Proksch et al. (2015). Here we briefly summarize the methodology of the casting and processing procedure.

The snow samples were cast using Diethly-Phthalate (DEP) to preserve the snow structure. The casting procedure as well as an accuracy analysis of cast and not-cast samples are described in Heggli et al. (2009). In the cold lab, the samples were scanned with a nominal resolution (voxel size) ranging from 10 µm for new snow to 20 µm for depth hoar. The size of the evaluated volumes ranged from 67 mm^3 for CT-1 and CT-2 ($512 \times 512 \times 256$ voxel with 10 µm voxelsize) to 917 mm^3 for CT-3 ($512 \times 512 \times 600$ voxel with 18 µm voxel size). The sizes of the evaluated volumes were chosen much larger than the representative elementary volume (REV) in order to obtain reliable results from the correlation functions. The REV required to derive reliably density estimates from CT measurements was found to be between 2 and 4 mm^3 (Kaempfer et al., 2005).

TCD
9, 6061–6123, 2015

The 3-D-gray-scale images, which resulted from the scans, were filtered using a Gaussian filter (sigma = 1 voxel, filter kernel support = 2 voxel). The smoothed images were then segmented into binary images. For snow/air segmentation, the intensity threshold was chosen at the minimum between the DEP peak and the air peak in the histograms of the gray-scale images.

3.4 Processing the SnowScat data and CPD retrival

The frequency-domain raw data, measured by the SSI, were windowed to select a specific frequency band of 2 GHz bandwidth which was then focused into the single-look-complex (SLC) format (details in Leinss et al., 2015). The pixels of an SLC acquisition represent the complex-valued backscatter amplitude profiles $S_{\mathrm{pol}}(r, \theta_0, az)$ along range r. The phase of the complex signal contains information about the signal propagation delay. The uncalibrated CPD was calculated from the complex-valued, copolar coherence defined as

$$\gamma_{\mathrm{VV,HH}} \cdot e^{i\phi_{\mathrm{CPD}}}(\theta_0, az) = \frac{\langle S_{\mathrm{VV}} \cdot S^*_{\mathrm{HH}} \rangle}{\sqrt{\langle |S_{\mathrm{VV}}|^2 \rangle \cdot \langle |S_{\mathrm{HH}}|^2 \rangle}}. \quad (22)$$

The ensemble averages of about 150–300 range-pixels contained in the antenna footprint are indicated by $\langle \cdot \rangle$, and * is the complex conjugation. The magnitude of the coherence, $\gamma_{\mathrm{VV,HH}}$, is a measure for volume scattering and ranges ideally between 0 (only volume scattering) and 1 (only surface scattering). However, the coherence is reduced by system noise and rough surfaces. For noise and speckle reduction, the copolar coherences of different azimuth-subsectors with the same incidence angle were averaged. The phase $\phi_{\mathrm{CPD}} = \phi_{\mathrm{VV}} - \phi_{\mathrm{HH}}$, obtained from the averaged coherence, is the CPD as defined in Eq. (15).

TCD
9, 6061–6123, 2015

3.5 SnowScat calibration

The measured radar signal was calibrated by an internal calibration loop of the SSI to compensate system drifts. However, some polarization dependent signal delay still originated from the connectors of the antenna feeding cables and from the antennas themselves due to the polarization-dependent beam-pattern. In order to calibrate external offsets and drifts, the CPD was calibrated with two metallic targets.

The primary calibration target was a metallic sphere with a diameter of 25 cm mounted on a wooden pole for the duration of the experiment. The sphere can be located in Fig. 5 next to the SSI. A secondary target, a metallic plate was located behind trees close to sector 2. A third calibration target, a dihedral reflector, was installed during the setup phase of the experiment. The correct pointing direction to locate the sphere was determined with a precision of ±0.5° by 2-D-scans in elevation and azimuth. The 2-D-scans showed that a possible systematic error of the CPD, caused by imprecise alignment, can be estimated to be below ±10°.

The theoretical CPD measured from a sphere (or plate) is expected to be zero due to the target symmetry. The sphere was measured every four hours and was used as a reference during the whole duration of the experiment. The plate was installed from October 2011 until June 2013 and was used to validate the calibration done with the sphere. The CPD measured for a dihedral reflector should be 180°. The dihedral reflector was measured once, on 9 December 2009, to verify the processing sequence of the SnowScat raw data.

The CPD determined for the sphere, $\mathrm{CPD}_{\mathrm{REF}}$, was used as a reference and was subtracted from the uncalibrated CPD measurements of snow, $\mathrm{CPD}_{\mathrm{uncal.}}$, to obtain calibrated results:

$$\mathrm{CPD}_{\mathrm{cal.}}(f) = \mathrm{CPD}_{\mathrm{uncal.}}(f) - \mathrm{CPD}_{\mathrm{REF}}(f). \quad (23)$$

Phase unwrapping was performed for the uncalibrated CPD and the reference CPD if necessary.

TCD
9, 6061–6123, 2015

To reduce the noise of the reference measurements as much as possible, the reference, CPD_{REF}, was determined as follows: Time series $CPD_{REF}(t)$ were obtained for 21 different frequencies in order to sample the entire frequency spectrum between 9.2 and 17.8 GHz of the instrument. The time series were smoothed with a median filter of 4 days which preserved phase jumps in the signal. After temporal filtering, a frequency-dependent 4th order polynomial was fitted over the measured frequency spectrum of each acquisition to provide some noise reduction in the frequency domain.

The reference data are shown for all four seasons in Fig. 6. The solid black line shows the (frequency-dependent) reference, CPD_{REF}, for f = 13.5 GHz. Individual measurements of the sphere as well as measurements of the metallic plate are shown as dark and light gray solid dots below the black line.

In the third season, between 18 November 2011 and 20 January 2012, the pointing direction (elevation angle) to the sphere was misaligned by 2°. Therefore, the reference CPD was corrected by a frequency dependent offset to keep the CPD continuous at the start and the end of the period of misalignment.

The deviation of the raw-data of the sphere from the reference, $\Delta CPD = CPD(f) - CPD_{REF}(f)$, is shown in the lower panels for each season as scattered dots for each of the 21 analyzed frequencies. The root-mean-square-error, RMSE, was below 4° for the full frequency spectrum and is given for each seasons next to the graph. The error of the reference, $CPD_{REF}(f)$, which includes systematic and statistic errors, is estimated to be below 15°.

3.6 Selecting valid acquisitions

Invalid acquisitions were removed before the analysis with the help of the calibration data. Acquisitions were classified as invalid if the CPD or the Radar Cross Section (RCS) of the reference targets deviated too far from the expected values or if the temporal trend of the sphere and the plate-target were not in agreement. In the two seasons before 18 November 2011, where the plate target was not installed yet, the sphere showed very stable results therefore the data was considered as valid. For sector 2,

TCD
9, 6061–6123, 2015

which was located between trees, some subsectors at the left and right hand side were disturbed by trees (Leinss et al., 2015, Fig. 3) and were therefore excluded from the analysis.

4 Analysis

In the following sections, four years of CPD time series measurements and the derived anisotropies are presented. First, the CPD time series are discussed with respect to meteorological data and snow characteristics. Then, the temporal evolution of the average anisotropy is derived from CPD and snow depth measurements. The CPD measurements at different incidence angles and frequencies are used together with the obtained anisotropy to validate the electromagnetic model. For three dates anisotropy measurements are compared with anisotropy data from computer tomography. The potential of CPD measurements for fresh snow detection is discussed. Finally, we compare the CPD measurements with satellite data and discuss if the underlying soil affects the CPD measurements and the anisotropy of snow.

4.1 Time series of CPD

Four years of CPD time series are plotted in Figs. 7–10 together with meteorological data. Shown are the meteorological parameters snow depth (sensor SDAT1), air- and soil temperature (sensor SDAT1 and SMT) as well as soil moisture (sensor SMT) and snow density. The snow density was determined by dividing SWE, as determined in (Leinss et al., 2015), by the snow depth measured by the sensor SDAT1. Manual density measurements obtained in the snow pit are also shown.

The polarimetric radar measurements are plotted in the lower panels of Figs. 7–10. The CPD ($= \phi_{VV} - \phi_{HH}$) measured by the SSI is plotted for different incidence angles, θ_0, and frequencies, f. The lowest panel shows the co-polar coherence $\gamma_{VV,HH}$.

TCD
9, 6061–6123, 2015

The dark gray shading in Figs. 7–10 indicates the period of snow melt in April and May. Snow free conditions are indicated by a light gray shading in autumn and May/June. In the following paragraphs we summarize the main characteristics observed during the four winter seasons.

A common characteristic which was found in all four seasons was a rising CPD during snow fall. The CPD reached its maximum typically a few days after snowfall ended. During periods of cold temperatures without much fresh snow, the CPD decreased gradually, as long as temperatures were well below 0 °C. During snow melt, the CPD was close to zero as the penetration of microwaves into the wet snow pack is inhibited. Soil moisture correlates well with snow melt, but does not show any influence on the CPD, even when the soil was not frozen in early winter.

The copolar coherence, $\gamma_{VV,HH}$, is shown for the highest incidence angle ($\theta_0 = 60°$) where it is most sensitive to volume scattering. During dry snow conditions, $\gamma_{VV,HH}$ ranges from 0.4 to 0.7 (depending on frequency). Only at 16.8 GHz at 60° the coherence was found to be lower during winter (≈ 0.4) compared to snow free conditions ($\gamma_{VV,HH} \approx 0.5...0.6$), which indicates some weak scattering in the snow volume. The highest values of $\gamma_{VV,HH} = 0.7...0.8$ were measured during snow melt, where the microwave penetration depth is very weak (a few cm) and scattering occurs at the snow surface. After all snow has melted, the coherence decreased to $\approx 0.5...0.6$ and some volume scattering occurs at the low vegetation.

The four analyzed winter seasons showed quite different snow conditions. In the following paragraphs, we provide an interpretation of the measured CPD time series with respect to snow properties which were observed in the field and which were documented in Lemmetyinen et al. (2013, p. 399(49)).

The winter of 2009–2010 was characterized by mild temperatures until mid of December which caused a delayed freezing of the soil compared to average years. Snow accumulation happened gradually and the mild temperatures lead to snow densities of 0.2 g cm^{-3} in early winter. Due to warm temperatures, depth hoar was largely absent and melt-refreeze events caused the formation of a crust at the bottom of the snow

TCD
9, 6061–6123, 2015

pack. Later in winter, two major snow fall events occurred. The first happened during early February after which the CPD increased by more than 50°. The second major snow fall occurred during the night from 2 to 3 March, where a fast rise in temperatures together with 20 mm precipitation caused strong snow settling. Consequently an abrupt increase of the CPD of about 20° happened during the night followed by a total increase of more than 50° within the 5 following days.

The winter of 2010–2011 was characterized by very cold temperatures and a relatively thin snow cover. The strong temperature gradients lead to a distinct layer of depth hoar. The slightly negative CPD in December indicates a weak vertical anisotropy in the snow pack. From January until March, the CPD increased with snow fall but was disrupted by a period of very cold temperatures in February during which the CPD decreased by 50°.

The winter of 2011–2012 was characterized by initially exceptionally mild temperatures and late but intense snow fall during December. The weak temperature gradient from mid December until mid January caused almost no recrystallization into vertical structures. Therefore, a thick layer of horizontally oriented, settled fresh snow was preserved and a maximum CPD of +135° was observed at 7 January, 9 days after 20 cm of fresh snow. Almost no depth hoar was observed due to the insulating effect of the thick snow pack. The extremely large phase differences disappeared relatively quickly during very cold air temperatures between −15 and −35 °C in the second half of January and early February and the CPD even changed sign, so that a minimum CPD of −30° was observed at 9 February. After various snowfall events, the negative phase differences disappeared. At 12 April, the snow surface melted and refroze afterwards. A significant drop in the copolar coherence (Fig. 9) indicates increased volume scattering or even residual melt water in the snow pack. During the time around 12 April, when the snow surface was wet snow, the CPD dropped for a few days to zero but recovered afterwards during a short period of negative temperatures before snow melt.

The winter of 2012–2013 was again characterized by very mild temperatures but early and heavy snowfall during November, followed by three additional major snowfall

TCD
9, 6061–6123, 2015

events, which caused a very clear peak-like signal in the CPD. In February, after the last heavy snow fall, a CPD of more than +100° was reached. From March until mid April, no snow fall was present and low temperatures caused a strong recrystallization for a period of 6 weeks, after which a minimum CPD of −60° was observed. With the onset of snow melt, the CPD jumped to zero due wet snow and the resulting weak microwave penetration depth.

4.2 Estimation of the average anisotropy of snow

The developed electromagnetic model from Sect. 2 is free of fit-parameters. Therefore, the measured copolar phase, $\mathrm{CPD}_{\mathrm{meas.}}$, can be inverted to get a CPD-based estimate for the depth-average anisotropy $A_{\mathrm{avg}}^{\mathrm{CPD}}$.

The average anisotropy can be estimated, because the CPD shows only a weak density dependence for the density range of seasonal snow (Bormann et al., 2013). Between densities of 0.15 and 0.4 g cm^{-3}, the CPD varies by less than 20 % as shown by Fig. 3a.

For the analysis in this section, we assumed that the snow pack observed at different incidence angles consisted of a single layer with constant anisotropy A. Equation (19) can then be used to model the CPD for a given frequency f, incidence angle θ_0, snow depth ΔZ, and snow density ρ. For every measurement time t, the depth-averaged, CPD-based estimate $A(\theta_0, f)$ follows for each incidence angle θ_0 and frequency f by minimization of the difference

$$|\mathrm{CPD}_{\mathrm{meas}}(t, \theta_0, f) - \mathrm{CPD}_{\mathrm{model}}(A, \theta_0, f)|. \quad (24)$$

The estimated anisotropy, $A_{\mathrm{avg}}^{\mathrm{CPD}}(t)$, for a given time is then computed by averaging the estimated values $A(\theta_0, f)$ over all incidence angles and frequencies. The standard deviation for each time follows directly from the difference between $A_{\mathrm{avg}}^{\mathrm{CPD}}(t)$ and the estimates $A(\theta_0, f)$ for each θ_0, and f.

TCD
9, 6061–6123, 2015

The input parameters to estimate $A_{\mathrm{avg}}^{\mathrm{CPD}}(t)$ are snow depth and density as shown in Figs. 7–10. Radar measurements $\mathrm{CPD}_{\mathrm{meas}}(t, \theta_0, f)$ at 16 different frequencies between 10 and 17 GHz were used. For estimation of $A_{\mathrm{avg}}^{\mathrm{CPD}}(t)$ we used only three incidence angles $\theta_0 = 40...60^{\circ}$, since the CPD measurements with the smallest incidence angle ($\theta_0 = 30^{\circ}$) showed the highest sensitivity to calibration errors and other uncertainties.

The processing chain to determine the anisotropy is shown in the block diagram in Fig. 11. Time series of the estimated anisotropy are shown in Fig. 12. The average standard deviation of $\sigma_A \approx 0.005$ is well below the range of the anisotropy between −0.05 and +0.2. The standard deviation varies with snow depth and is shown as a gray bar below the anisotropy.

4.3 Incidence angle and frequency dependence

The larger the incidence angle, the better are the vertically polarized microwaves aligned with the optical axis of anisotropic snow. The CPD must therefore increase with increasing incidence angle. This has already been observed in the CPD time series plotted for different incidence angles in the middle panel of Figs. 7–10.

The electromagnetic model presented in Sect. 2 predicts a nonlinear incidence angle dependence due to refraction in the snow pack (Fig. 3). To verify the nonlinear incidence angle dependence, we selected five dates spread over the four winter seasons to cover the maximum available range of CPDs. For each date we used the measured snow density, ρ, and the CPD-based anisotropy, $A_{\mathrm{avg}}^{\mathrm{CPD}}$, to model the expected incidence angle dependence. A comparison of modeled and measured incidence angle dependence is shown in Fig. 13 (left) for the five selected dates.

The CPD is modeled to be proportional to the depth of a snow pack which is transparent for microwaves. The deeper the snow and the higher the frequency, the more wavelengths "fit" into the snow volume and the higher is the expected phase difference. This frequency dependence is described by Eq. (19) which shows a linear frequency dependence ($\propto \lambda^{-1}$). Larger CPD values were indeed measured for higher frequencies

TCD
9, 6061–6123, 2015

as it is shown for f = 10.2, 13.5 and 16.8 GHz in the 2nd-last panel of Figs. 7–10. For a more quantitative insight, we plotted the CPD measured for 16 different frequencies in Fig. 13 (right). The CPD was plotted for the same five dates shown in Fig. 13 (left). As expected, the CPD shows approximately a linear dependence on frequency.

In order to get a better quantitative measure how well the electromagnetic model fits to the measured data, we did a statistical analysis and compared the modeled phase difference, $\mathrm{CPD}_{\mathrm{model}}(A_{\mathrm{avg}}^{\mathrm{CPD}}(t), \theta_0, f)$, according to Eq. (19), with the measured phase difference, $\mathrm{CPD}_{\mathrm{meas.}}(t, \theta_0, f)$. The mean deviation, as well as the standard deviation of $\mathrm{CPD}_{\mathrm{model}} - \mathrm{CPD}_{\mathrm{meas.}}$, were calculated over all acquisitions acquired during dry snow conditions separately for each incidence angle θ_0 and for each frequency f.

The mean deviation is plotted over frequency and for each incidence angle in Fig. 14. The error bars indicate the standard deviation. The mean deviation is about ±4° (black dots in Fig. 14) and is almost always within the standard deviation (error bars). Only for $\theta = 60^\circ$ and $f > 14$ GHz, we measure larger deviation up to +8°. Figure 14 shows that neither large deviations from the expected incidence angle dependence nor large deviations from the linear frequency dependence were found. The deviations of $\mathrm{CPD}_{\mathrm{meas}}$ from the $\mathrm{CPD}_{\mathrm{model}}$ are within the estimated calibration accuracy of ±15°.

As measured and modeled data agree within a few degree, we conclude that our electromagnetic model is able to explain the observed CPD by considering snow as an optically anisotropic medium. The linear dependence on frequency confirms our assumption that the CPD is a volumetric property of snow.

4.4 Validation with computer tomography

For validation we compared the CPD-based estimates $A_{\mathrm{avg}}^{\mathrm{CPD}}$ to tomography based estimates $A_{\mathrm{avg}}^{\mathrm{CT}}$ obtained from in-situ snow measurements. The dates, when the samples for computer tomography analysis were taken from the three snow pits, CT-1, CT-2, and CT-3, are indicated in Figs. 9, 10, and also in Fig. 12 as dashed vertical lines. Four

TCD
9, 6061–6123, 2015

examples of 3-D images of snow samples of about 2 cm height are shown in Figs. 15 and 16.

In order to obtain the anisotropy from the computer tomography data, the binary 3-D images were analyzed by means of spatial correlation functions according to Löwe et al. (2011). Exponential correlation lengths, $p_{\mathrm{ex},x}$, $p_{\mathrm{ex},y}$, and $p_{\mathrm{ex},z}$, were derived from the correlation functions as described by Mätzler (2002). The anisotropy determined by computer tomography, A_{CT}, is defined analogue to Eq. (1). Due to the symmetry in the x and y direction, $p_{\mathrm{ex},x}$ and $p_{\mathrm{ex},y}$ were averaged:

$$A_{\mathrm{CT}} = \frac{(p_{\mathrm{ex},x} + p_{\mathrm{ex},y}) - 2p_{\mathrm{ex},z}}{\left[\frac{1}{2}(p_{\mathrm{ex},x} + p_{\mathrm{ex},y}) + p_{\mathrm{ex},z}\right]}. \quad (25)$$

The anisotropy was determined with a vertical resolution of 1–2 mm, depending on snow grain size, for the entire snow profile. The obtained anisotropy profiles are shown in Fig. 17. For comparison, we added horizontal lines, which show the average anisotropy, $A_{\mathrm{avg}}^{\mathrm{CT}}$, determined from computer tomography and the average anisotropy, $A_{\mathrm{avg}}^{\mathrm{CPD}}$, determined from the CPD.

For the first two profiles, CT-1 and CT-2, the difference in anisotropy is remarkably small and agrees within values of +0.008 and −0.004, or +4 and −8 %. However, for the third profile, CT-3, a larger difference of +0.08 was observed. The difference might originate from a very sparse sampling of the top snow layers (see Fig. 17, bottom left), as taking samples was difficult due to soft fresh snow. No samples could be taken from the top 4 cm. We can exclude limited penetration as a reason for the difference, despite occurring warm temperatures a few days before, because the copolar coherence (Fig. 10) and the temporal coherence (Leinss et al., 2015, Fig. 19) did not show any anomaly. However, we can not exclude the fact, that the assumption of oriented spheroids in our model is a too strong assumption for the very dendritic shape of fresh fluffy snow.

The vertical structure of the anisotropy profiles agrees to our expectation regarding the meteorological conditions as described in the caption of Fig. 17. In the anisotropy

TCD
9, 6061–6123, 2015

profiles vertical structures were found in the older snow layers, as it is expect for snow recrystallized by temperature gradient metamorphism. In contrast to the old layers, the top layers show horizontally aligned structures as we expect it to be the case for fresh snow. The fact, that fresh snow is related to horizontal structures and therefore to a positive CPD, makes it possible to use the CPD for detection of fresh snow.

4.5 Correlation between fresh snow and a positive CPD

The settling of snow has been shown to be responsible for an increasingly positive anisotropy (Löwe et al., 2011). According to our theory, increasing anisotropies cause an increase of the CPD. This makes it possible to use a change in CPD to detect fresh snow as done in Leinss et al. (2014) using satellite data. However, the CPD does not increase simultaneously with the accumulation of fresh snow, but increases with a time-lag τ as the snow first has to settle until an increased CPD can be observed. Further, the CPD decreases during periods of cold temperatures due to temperature gradient metamorphism. Therefore an increase of the CPD is not expected to be exactly proportional to an increase in snow depth.

In this section we analyze the correlation between fresh snow and a change in CPD. The correlation is defined as

$$R = \mathrm{corr}\{\mathrm{CPD}(t+\tau) - \mathrm{CPD}(t+\tau-\Delta T), \\ \mathrm{SD}(t) - \mathrm{SD}(t-\Delta T)\}, \quad (26)$$

where R is the Pearson-correlation coefficient. The time ΔT is the time difference between two measurements and corresponds e.g. to the repeat time of satellite acquisitions. The sampling interval ΔT needs to be large enough in order to give fresh snow some time for settling. However, the sampling time should not be too large, as minor snow fall events might be missed, and also snow metamorphosis will reduce measured values of the positive CPD changes which are typical for fresh snow.

The scatter plot in Fig. 18 (top) shows the correlation between the depth of fresh snow within 12 days and the corresponding change in CPD measured with a time-lag

TCD
9, 6061–6123, 2015

of 3.5 days. The scatter plot is shown for the best correlation, $R = 0.75$, which was found for different values of ΔT and τ. The correlation coefficient R is shown for all tested values of Δt and τ in the contour plot of Fig. 18 (top right). The red cross marks the pair with the highest correlation coefficient.

The range of optimal sampling intervals, ΔT, can be derived from the contour plot shown in Fig. 18. The plot shows that the optimal ΔT is between 9 and 15 days. We analyzed all frequencies and incidence angles and the best correlation coefficients, which ranged between 0.65 and 0.75, were always found for $\Delta T = 11 \pm 3$ days and a time-lag of $\tau = 3.0 \pm 0.5$ days.

The optimal sampling interval ΔT matches the 11 day orbit repeat time of TerraSAR-X. Using time series of TerraSAR-X, a CPD change of +10 to +15° per 10 cm of fresh was observed at 9.65 GHz at an incidence angle of 33° (Leinss et al., 2014). From these results we would expect that the CPD changes by 40–60° at the central frequency of the SSI of 13.5 GHz at $\theta_0 = 60°$. Here we observed a change in CPD of 38° per 10 cm of fresh snow at 13.5 GHz which fits well with respect to the uncertainty $R = 0.74$ of Fig. 18 (top left).

The availability of accurate time series of the SWE measurements published in Leinss et al. (2015) made it also possible to check if a correlation exists between ΔSWE and ΔCPD. The lower two graphs of Fig. 18 show an example for the correlation. The best correlations ($R \approx 0.65...0.8$) were found for a sampling interval of $\Delta T = 10 \pm 3$ days with a time-lag of $\tau = 2.2 \pm 0.3$ days. The correlation with ΔSWE is slightly better compared to the correlation with ΔSD.

4.6 Comparison with satellite data

The CPD observed by the ground-based SnowScat instrument could also be measured from space with the satellite TerraSAR-X (TSX). Spatial and temporal correlations between the CPD and snow depth were published by Leinss et al. (2014). Fig. 19 compares phase differences measured by TSX for the two seasons 2011–2012 and 2012–2013. The space-borne measurements show the same trends as the ground based

TCD
9, 6061–6123, 2015

measurements. However, the phase differences observed by TSX are about a factor 2 smaller than the CPD measured with the SSI (scatter plot in Fig. 19). The reason is very likely, that the TSX data were obtained from large open areas. In the large areas about 30 % less snow depth was measured (cf. Fig. 3 in Leinss et al., 2014), probably due to a stronger wind exposition compared to the more wind-protected forest clearing, where the SSI was located. Wind might also be a reason for disturbed snow settling as wind drifted snow crystals show a different microstructure than undisturbed settled snow. The lower snow depth and the stronger wind exposition might explain, why smaller phase differences were measured. Some residual vegetation and trees which were contained in the large areas observed by TSX, also decreased the measured CPD due to spatial averaging.

4.7 Effect of underlying soil

Sector 2, as shown in Fig. 5, was covered with an metallic mesh by August 2011 to isolate purely snow specific radar signatures from effects of the underlying soil. In the winter 2011/12 strong ice built up on the mesh causing high backscattering. However, we did not observe any effect on the CPD. To prevent the build up of an ice crust in the next season, the mesh was cleared from ice on 10 December 2012. The removal of the ice crust in the season 2012/13 did again not much affect the measured CPD, and no large differences between the soil sector and the mesh-sector were found. We could speculate, that slightly larger CPD values measured between January and April 2013 might indicate the missing of a layer of vertical oriented depth hoar crystals, but the deviation could also originate from slightly different snow conditions of the two sectors. Still, the good agreement between the measurements of the soil sector and the measurements from the metallic mesh confirms again that the measured CPD is almost purely a signal resulting from the snow volume. Whereas the CPD signal is caused by the snow volume, temperature gradient metamorphism alters the anisotropy of snow and the temperature gradient is partially determined by the temperature of the underlying soil.

TCD
9, 6061–6123, 2015

5 Conclusions

In this paper, we demonstrated a contact-less and destruction-free technique for monitoring the anisotropy of snow. The anisotropy was determined by analyzing copolar phase differences (CPD) of ground based radar acquisitions. A theoretical framework was provided, which describes the anisotropy as vertically aligned, oblate or prolate spheroidal ice grains. Maxwell–Garnett type mixing formulas were then applied to determine the effective permittivity tensor to describe the birefringent properties of snow. To ensure a unified microstructure characterization with previous work, we have shown that this model based on identical spheroidal inclusions is identical to a more general approach to the effective permittivity tensor based on correlation functions. Using the permittivity tensor, which determines the birefringence of snow, we calculated the wave propagation according to anisotropic optics. The propagation delay difference of orthogonally polarized microwaves was measured by the CPD which was then used to determine the structural anisotropy of snow.

Four years of polarimetric radar data acquired by the SnowScat Instrument, installed at a test site near the town of Sodankylä, Finland were analyzed. The temporal evolution of the depth-averaged anisotropy of the snow pack could be observed and the anisotropy, ranging between −0.05 and +0.25, could be determined with a standard deviation of 0.005. Copolar phase differences ranging from −30° to +135° were measured for 50–60 cm deep snow at a frequency of 13.5 GHz. The electromagnetic model was tested at different frequencies between 10 and 17 GHz, and for different incidence angles between 30 and 60° in order to analyze deviations from measured data. Only small deviations of 5–10° were found and the expected linear frequency dependence could be confirmed. The linear frequency dependence verifies our assumption that the CPD is a volumetric property of snow determined by its structural anisotropy.

The estimated anisotropies were validated by micro-computed tomography (μCT) measurements for which the anisotropy was determined from two-point correlation functions for three dates. The depth-averaged anisotropy of two of the μCT-derived

TCD
9, 6061–6123, 2015

anisotropy profiles agreed within 4 and 8 % with our measurements. For one sample we found a larger deviation of which origin could only be hypothesized to result from missing snow samples or from too coarse assumptions of the Maxwell–Garnett mixing formulas.

In addition, we investigated the potential of how a changing CPD can be used to detect fresh snow and the accumulation of the water equivalent of snow (SWE). A weak correlation was found and an optimal acquisition interval of 8–15 days was determined to detect the depth of fresh snow. It was observed that the evolution of the CPD shows a delay of about 2–3 days compared to the evolution of snow depth, which indicates an average settling time of a few days.

The CPD measurements obtained from the ground based instrument SnowScat were compared with space borne acquisitions by TerraSAR-X. Both sensors showed the same temporal trend. However, the CPD observed by TerraSAR-X was about a factor of two smaller than the measurements done by SnowScat. A reason could be the higher snow accumulation on the forest clearing where the SnowScat instrument was located. Stronger wind exposition and the existence of some vegetation for the areas observed by TSX are assumed to be a reason for the smaller measured CPD values.

The possibility to observe the anisotropy of the snow pack by remote sensing techniques opens a wide field of applications. Detection of fresh snow was already discussed in the previous section. Determination of the thickness of a firn layer on glaciers might be possible, when correct assumption for the anisotropy and the scattering properties of firn are made and when frequencies which penetrate deep enough into firn are used.

Another interesting application is using CPD measurements as a proxy for the thermal conductivity of the snow pack. As the dielectric anisotropy can be exactly related to the anisotropy employed for parametrization of the thermal conductivity (Löwe et al., 2013) it seems feasible to aim at a proxy for the thermal conductivity from radar measurements, given a reasonable assumption about the mean density. Thereby, the anisotropy would reflect variations in the metamorphic state of the snow pack since

TCD
9, 6061–6123, 2015

increasing vertical structures are indicative of depth hoar and of an increased vertical thermal conductivity. This is particularly interesting for permafrost regions, where large vertical structures often arise from high temperature gradients in the thin snow pack in early-winter. Depth hoar, with its large ice crystals and low snow density close to vegetation and soil in turn, is not only important for the survival of many rodents (Bilodeau et al., 2013) but also very important in understanding the backscattering signal from snow (King and Derksen, 2015).

The large observation time spanning four winter seasons with a sampling interval of four hours builds a unique data source to study the evolution of the anisotropy of snow. The data and the demonstrated measurement technique might lead to improved snow models, in order to gain a deeper insight into the growth mechanisms of anisotropic snow crystals. Understanding the microscopic anisotropy of snow enhances the understanding of macroscopic anisotropic properties such as thermal conductivity, mechanical stability and electromagnetic properties. The developed method to measure snow anisotropy, its good agreement with ground-based μCT measurements, and the fair agreement with satellite-based radar measurement, provide a unique opportunity to improve snow models, and globally sense the metamorphic state of the snow pack.

Appendix: Re-derivation of Maxwell–Garnett equations via correlation functions

In Rechtsman and Torquato (2008) an exact series expansion of the dielectric permittivity of arbitrary anisotropic two-phase materials was derived and related to the n-point correlation functions of the material. If the series is truncated at $n = 2$, the final result (Rechtsman and Torquato, 2008, Eq. 16) can be solved for the diagonal components, $\varepsilon_{\mathrm{eff},i}$, $i = x, y, z$, of the effective permittivity tensor which can be written in the form

$$\varepsilon_{\mathrm{eff},i} = \varepsilon_q + \varepsilon_q \phi_p \frac{(\varepsilon_p - \varepsilon_q)}{\varepsilon_q + (1-\phi_p)\left[\frac{1}{3} - \frac{U_i}{3\phi_p\phi_q}\right](\varepsilon_p - \varepsilon_q)}. \quad \text{(A1)}$$

TCD
9, 6061–6123, 2015

The permittivities and volume fractions of the two phases which compose the microstructure are denoted by $\varepsilon_p, \varepsilon_q$ and ϕ_p, ϕ_q, respectively. The quantities U_i in Eq. (A1) are related to integrals over the two-point correlation function $C(\boldsymbol{r})$ as defined in Löwe et al. (2013, Eq. 1). In the lowest order of frequency f, contributions from scattering in the effective permittivity can be neglected (cf. Rechtsman and Torquato, 2008, Eqs. C3, C4). Then the U_i have vanishing imaginary part and are given by

$$U_x = U_y = \frac{3}{4\pi} \int_{\mathbb{R}^3} d^3r \, \frac{1}{r^3} \left(-1 + \frac{3}{2} \sin^2\theta \right) C(\boldsymbol{r}) \tag{A2}$$

$$U_z = \frac{3}{4\pi} \int_{\mathbb{R}^3} d^3r \, \frac{1}{r^3} \left(-1 + 3\cos^2\theta \right) C(\boldsymbol{r}) \tag{A3}$$

Here $r = |\boldsymbol{r}|$ is the magnitude of $\boldsymbol{r}$ and θ denotes the angle between the vertical z axis and $\boldsymbol{r}$.

If the microstructure is (statistically) transversly isotropic, it is reasonable to assume a "spheroidal symmetry" of the correlation function, viz $C(\boldsymbol{r}) = C(r/\sigma(\theta))$ with $\sigma(\theta) = 2a_x[1 - (1 - a_x^2/a_z^2)\cos^2\theta]^{1/2}$ as used in Löwe et al. (2013). Under this assumption, the singular integrals in A2 can be calculated as shown in Torquato and Lado (1991). The results can be inserted into the square brackets in A1 leading to

$$\left[\frac{1}{3} - \frac{U_x}{3\phi_p\phi_q} \right] = Q \tag{A4}$$

$$\left[\frac{1}{3} - \frac{U_z}{3\phi_p\phi_q} \right] = 1 - 2Q \tag{A5}$$

where the anisotropy parameter Q is defined in Löwe et al. (2013, Eq. 4) or Torquato (2002, Eqs. 17.30/17.31). Using the definition of depolarization factors from Torquato (2002, Eq. 17.25), noting their relation to Q from Torquato (2002, Eq. 17.29) on one

TCD
9, 6061–6123, 2015

hand, and their equivalence to the definition of N_i from Eq. (8) and from the last paragraph of Sect. 2.2 on the other hand we end up with

$$\varepsilon_{\mathrm{eff},i} = \varepsilon_q + \varepsilon_q \phi_p \frac{(\varepsilon_p - \varepsilon_q)}{\varepsilon_q + (1-\phi_p) N_i (\varepsilon_p - \varepsilon_q)}. \quad \text{(A6)}$$

We note here that Torquato (2002, Eq. 17.25) contains a typo. Specifying p to be the ice phase and q to be the air phase in Eq. (A6), gives $\varepsilon_q = \varepsilon_{\mathrm{air}}$, $\varepsilon_p = \varepsilon_{\mathrm{ice}}$, $\phi_p = f_{\mathrm{vol}}$ in the notation from Sect. 2.2, and thus Eq. (A4) coincides with the Maxwell–Garnett result Eq. (6a).

Acknowledgements. The in situ data collection was supported by the European Space Agency activity "Technical assistance for the deployment of an X- to Ku-band scatterometer during the NoSREx experiment" (ESA ESTEC Contract no. 22671/09/NL/JA/ef) (Lemmetyinen et al., 2013). The staff at FMI-ARC is acknowledged for the collection of in situ data. We thank Anna Kontu for providing the meteorological data and her excellent local expertise concerning all experimental details at the test site. Special thank goes to Jouni Pulliainen from FMI for the initiative of setting up a test site which provides a unique amount and diversity of meteorological data and snow measurements. We thank Christian Mätzler for adapting his model of the relative permittivity of snow in order to make it valid for high snow densities up to solid ice.

References

Alley, R.: Texture of polar firn for remote sensing, Ann. Glaciol., 9, 1–4, 1987. 6063, 6076

Ao, C. O. and Kong, J. A.: Analytical approximations in multiple scattering of electromagnetic waves by aligned dielectric spheroids, JOSA A, 19, 1145–1156, 2002. 6070

Bilodeau, F., Gauthier, G., and Berteaux, D.: The effect of snow cover on lemming population cycles in the Canadian High Arctic, Oecologia, 172, 1007–1016, doi:10.1007/s00442-012-2549-8, 2013. 6095

Bohleber, P., Wagner, N., and Eisen, O.: Permittivity of ice at radio frequencies: Part II. Artificial and natural polycrystalline ice, Cold Reg. Sci. Technol., 83–84, 13–19, doi:10.1016/j.coldregions.2012.05.010, 2012. 6068

TCD
9, 6061–6123, 2015

Bormann, K. J., Westra, S., Evans, J. P., and McCabe, M. F.: Spatial and temporal variability in seasonal snow density, J. Hydrol., 484, 63–73, doi:10.1016/j.jhydrol.2013.01.032, 2013. 6086

Calonne, N., Geindreau, C., Flin, F., Morin, S., Lesaffre, B., Rolland du Roscoat, S., and Charrier, P.: 3-D image-based numerical computations of snow permeability: links to specific surface area, density, and microstructural anisotropy, The Cryosphere, 6, 939–951, doi:10.5194/tc-6-939-2012, 2012. 6064

Calonne, N., Flin, F., Geindreau, C., Lesaffre, B., and Rolland du Roscoat, S.: Study of a temperature gradient metamorphism of snow from 3-D images: time evolution of microstructures, physical properties and their associated anisotropy, The Cryosphere, 8, 2255–2274, doi:10.5194/tc-8-2255-2014, 2014. 6063, 6067

Chang, P., Mead, J., Knapp, E., Sadowy, G., Davis, R., and McIntosh, R.: Polarimetric backscatter from fresh and metamorphic snowcover at millimeter wavelengths, IEEE T. Antenn. Propag., 44, 58–73, doi:10.1109/8.477529, 1996. 6065

Cohn, E.: Das elektromagnetische Feld: Vorlesungen über die Maxwell'sche Theorie, S. Hirzel, Leipzig, Germany, 1900. 6068

Davis, R. E. and Dozier, J.: Stereological characterization of dry Alpine snow for microwave remote sensing, Adv. Space Res., 9, 245–251, doi:10.1016/0273-1177(89)90492-4, 1989. 6063

Fujita, S., Mae, S., and Matsuoka, T.: Dielectric anisotropy in ice Ih at 9.7 GHz, Ann. Glaciol., 17, 276–276, available at: http://www.igsoc.org:8080/annals/17/igs_annals_vol17_year1993_pg276-280.pdf, 1993. 6068

Fujita, S., Okuyama, J., Hori, A., and Hondoh, T.: Metamorphism of stratified firn at Dome Fuji, Antarctica: a mechanism for local insolation modulation of gas transport conditions during bubble close off, J. Geophys. Res.-Earth, 114, 1–21, doi:10.1029/2008JF001143, 2009. 6064

Fujita, S., Hirabayashi, M., Goto-Azuma, K., Dallmayr, R., Satow, K., Zheng, J., and Dahl-Jensen, D.: Densification of layered firn of the ice sheet at NEEM, Greenland, J. Glaciol., 60, 905–921, doi:10.3189/2014JoG14J006, 2014. 6064, 6076

Garrett, T. J., Fallgatter, C., Shkurko, K., and Howlett, D.: Fall speed measurement and high-resolution multi-angle photography of hydrometeors in free fall, Atmos. Meas. Tech., 5, 2625–2633, doi:10.5194/amt-5-2625-2012, 2012. 6065

TCD
9, 6061–6123, 2015

Guneriussen, T., Høgda, K. A., Johnsen, H., and Lauknes, I.: InSAR for estimation of changes in snow water equivalent of dry snow, IEEE T. Geosci. Remote, 39, 2101–2108, doi:10.1109/36.957273, 2001. 6071

Hallikainen, M., Ulaby, F., and van Deventer, T.: Extinction behavior of dry snow in the 18-to 90-GHz Range, IEEE T. Geosci. Remote, GE-25, 737–745, doi:10.1109/TGRS.1987.289743, 1987. 6071

Hashin, Z. and Shtrikman, S.: A variational approach to the theory of the effective magnetic permeability of multiphase materials, J. Appl. Phys., 33, 3125–3131, doi:10.1063/1.1728579, 1962. 6067

Heggli, M., Frei, E., and Schneebeli, M.: Instruments and methods snow replica method for three-dimensional X-ray microtomographic imaging, J. Glaciol., 55, 631–639, doi:10.3189/002214309789470932, 2009. 6079

Hendry, A., Mccormick, G., and Barge, B.: Ku-band and S-band observations of the differential propagation constant in snow, IEEE T. Antenn. Propag., 24, 521–525, doi:10.1109/TAP.1976.1141364, 1976. 6064

Hildebrand, T., Laib, A., Müller, R., Dequeker, J., and Rüegsegger, P.: Direct three-dimensional morphometric analysis of human cancellous bone: microstructural data from spine, femur, iliac crest, and calcaneus, J. Bone Miner. Res., 14, 1167–1174, 1999. 6066

Hogan, R. J., Tian, L., Brown, P. R. A., Westbrook, C. D., Heymsfield, A. J., and Eastment, J. D.: Radar scattering from ice aggregates using the horizontally aligned oblate spheroid approximation, J. Appl. Meteorol. Clim., 51, 655–671, 2012. 6065

Hörhold, M. W., Albert, M. R., and Freitag, J.: The impact of accumulation rate on anisotropy and air permeability of polar firn at a high-accumulation site, J. Glaciol., 55, 625–630, 2009. 6063

Izumi, K. and Huzioka, T.: Studies of metamorphism and thermal conductivity of snow, I, Low Temperature Science Series A, 33, 91–102, 1975. 6063

Jones, R.G.: The measurement of dielectric anisotropy using a microwave open resonator, J. Phys. D Appl. Phys., 9, 819–827, 1976. 6064

Kaempfer, T. U. and Schneebeli, M.: Observation of isothermal metamorphism of new snow and interpretation as a sintering process, J. Geophys. Res.-Atmos., 112, 1–10, doi:10.1029/2007JD009047, 2007. 6063

Kaempfer, T. U., Schneebeli, M., and Sokratov, S. A.: A microstructural approach to model heat transfer in snow, Geophys. Res. Lett., 32, l21503, doi:10.1029/2005GL023873, 2005. 6079

TCD
9, 6061–6123, 2015

King, J. and Derksen, C.: Retrieval of Tundra SWE Using airborne dual-frequency SAR (17.2/9.6 Ghz) and MEMLS-active, in: Proceedings IGARSS 2015, Milano, 2015. 6095
Lee, J.-S., Grunes, M., and De Grandi, G.: Polarimetric SAR speckle filtering and its implication for classification, IEEE T. Geosci. Remote, 37, 2363 –2373, doi:10.1109/36.789635, 1999. 6074
Leinss, S., Parrella, G., and Hajnsek, I.: Snow height determination by polarimetric phase differences in X-Band SAR data, IEEE J. Sel. Top. Appl., 7, 3794–3810, doi:10.1109/JSTARS.2014.2323199, 2014. 6064, 6065, 6072, 6076, 6090, 6091, 6092
Leinss, S., Wiesmann, A., Lemmetyinen, J., and Hajnsek, I.: Snow water equivalent of dry snow measured by differential interferometry, IEEE J. Sel. Top. Appl., 8, 3773–3790, doi:10.1109/JSTARS.2015.2432031, 2015. 6071, 6078, 6079, 6080, 6083, 6089, 6091, 6108
Lemmetyinen, J., Kontu, A., Leppänen, L., Pulliainen, J., Wiesmann, A., Werner, C., Proksch, M., and Schneebeli, M.: Technical assistance for the deployment of an X- to Ku-band scatterometer during the NoSREx experiment, Final report, Contract No. 22671/09/NL/JA/ef, Tech. rep., ESA ESTEC, Noordwijk, 2013. 6077, 6084, 6097
Li, L., Gaiser, P., Albert, M., Long, D., and Twarog, E.: WindSat passive microwave polarimetric signatures of the greenland ice sheet, IEEE T. Geosci. Remote, 46, 2622–2631, doi:10.1109/TGRS.2008.917727, 2008. 6064
Lüneburg, E. and Boerner, W.-M.: Statistical aspects of radar polarimetry, in: Fields, Networks, Computational Methods, and Systems in Modern Electrodynamics, edited by: Russer, P., and Mongiardo, M., vol. 97 of Springer Proceedings in Physics, Springer, Berlin, Heidelberg, 43–54, doi:10.1007/978-3-662-07221-9_5, 2004. 6074
Lomonaco, R., Albert, M., and Baker, I.: Microstructural evolution of fine-grained layers through the firn column at Summit, Greenland, J. Glaciol., 57, 755–762, doi:10.3189/002214311797409730, 2011. 6063
Löwe, H. and Picard, G.: Microwave scattering coefficient of snow in MEMLS and DMRT-ML revisited: the relevance of sticky hard spheres and tomography-based estimates of stickiness, The Cryosphere Discuss., 9, 2495–2542, doi:10.5194/tcd-9-2495-2015, 2015. 6070
Löwe, H., Spiegel, J., and Schneebeli, M.: Interfacial and structural relaxations of snow under isothermal conditions, J. Glaciol., 57, 499–510, 2011. 6063, 6064, 6066, 6089, 6090
Löwe, H., Riche, F., and Schneebeli, M.: A general treatment of snow microstructure exemplified by an improved relation for thermal conductivity, The Cryosphere, 7, 1473–1480, doi:10.5194/tc-7-1473-2013, 2013. 6063, 6064, 6067, 6070, 6094, 6096

TCD
9, 6061–6123, 2015

Lytle, V. and Jezek, K.: Dielectric permittivity and scattering measurements of Greenland firn at 26.5–40 GHz, IEEE T. Geosci. Remote, 32, 290–295, doi:10.1109/36.295044, 1994. 6064, 6065

Mätzler, C.: Applications of the interaction of microwaves with the natural snow cover, Remote Sensing Reviews, 2, 259–387, doi:10.1080/02757258709532086, 1987. 6063

Mätzler, C.: Microwave permittivity of dry snow, IEEE T. Geosci. Remote, 34, 573 –581, doi:10.1109/36.485133, 1996. 6067

Mätzler, C.: Autocorrelation functions of granular media with free arrangement of spheres, spherical shells or ellipsoids, J. Appl. Phys., 81, 1509–1517, doi:10.1063/1.363916, 1997. 6063

Mätzler, C.: Relation between grain-size and correlation length of snow, J. Glaciol., 48, 461–466, doi:10.3189/172756502781831287, 2002. 6063, 6066, 6089

Mätzler, C. and Wegmüller, U.: Dielectric properties of freshwater ice at microwave frequencies, J. Phys. D Appl. Phys., 20, 1623, available at: http://stacks.iop.org/0022-3727/20/i=12/a=013, 1987. 6068

Noel, V. and Chepfer, H.: A global view of horizontally oriented crystals in ice clouds from Cloud-Aerosol Lidar and Infrared Pathfinder Satellite Observation (CALIPSO), J. Geophys. Res.-Atmos., 115, 1–13, doi:10.1029/2009JD012365, 2010. 6065

Parrella, G., Hajnsek, I., and Papathanassiou, K.: Polarimetric decomposition of L-band PolSAR backscattering over the austfonna ice cap, IEEE T. Geosci. Remote, PP, 99, doi:10.1109/TGRS.2015.2477168, 2015. 6077

Pfeffer, W. T. and Mrugala, R.: Temperature gradient and initial snow density as controlling factors in the formation and structure of hard depth hoar, J. Glaciol., 48, 485–494, doi:10.3189/172756502781831098, 2002. 6063

Pinzer, B. R. and Schneebeli, M.: Snow metamorphism under alternating temperature gradients: morphology and recrystallization in surface snow, Geophys. Res. Lett., 36, 1–4, doi:10.1029/2009GL039618, 2009. 6063

Polder, D. and van Santen, J.: The effective permeability of mixtures of solids, Physica, 12, 257–271, doi:10.1016/S0031-8914(46)80066-1, 1946. 6067, 6068, 6070

Proksch, M., Löwe, H., and Schneebeli, M.: Density, specific surface area and correlation length of snow measured by high-resolution penetrometry, J. Geophys. Res.-Earth, 120, 346–362, doi:10.1002/2014JF003266, 2015. 6079

TCD
9, 6061–6123, 2015

Rechtsman, M. C. and Torquato, S.: Effective dielectric tensor for electromagnetic wave propagation in random media, J. Appl. Phys., 103, 084901, doi:10.1063/1.2906135, 2008. 6070, 6095, 6096

Riche, F., Montagnat, M., and Schneebeli, M.: Evolution of crystal orientation in snow during temperature gradient metamorphism, J. Glaciol., 59, 47–55, doi:10.3189/2013JoG12J116, 2013. 6063

Saleh, B. E. A. and Teich, M. C.: Fundamentals of Photonics, John Wiley and Sons, Inc., New York, 1991. 6071, 6072

Schleef, S., and Löwe, H.: X-ray microtomography analysis of isothermal densification of new snow under external mechanical stress, J. Glaciol., 59, 233–243, available at: http://www.scopus.com/inward/record.url?eid=2-s2.0-84881176673&partnerID=40&md5=2dd45ad6989d7ed1ff93abcecd78c02b, 2013. 6064

Schneebeli, M. and Sokratov, S.: Tomography of temperature gradient metamorphism of snow and associated changes in heat conductivity, Hydrol. Process., 18, 3655–3665, doi:10.1002/hyp.5800, 2004. 6063, 6066, 6076

Sihvola, A.: Mixing rules with complex dielectric coefficients, P. Soc. Photo.-Opt. Ins., 1, 393–415, doi:10.1023/A:1026511515005, 2000. 6067, 6068, 6069, 6070

Sihvola, A.: How strict are theoretical bounds for dielectric properties of mixtures?, IEEE T. Geosci. Remote, 40, 880–886, doi:10.1109/TGRS.2002.1006369, 2002. 6067, 6068

Torquato, S.: Random Heterogeneous Materials, Springer, New York, 2002. 6096, 6097

Torquato, S. and Lado, F.: Trapping constant, thermal conductivity, and the microstructure of suspensions of oriented spheroids, The J. Chem. Phys., 94, 4453–4462, doi:10.1063/1.460635, 1991. 6067, 6096

Tsang, L.: Polarimetic passive microwave remote sensing of random discrete scatterers and rough surfaces, J. Electromagnet. Wave., 5, 41–57, 1991. 6064

Tsang, L., Pan, J., Liang, D., Li, Z., Cline, D., and Tan, Y.: Modeling active microwave remote sensing of snow using dense media radiative transfer (DMRT) theory with multiple-scattering effects, IEEE T. Geosci. Remote, 45, 990–1004, doi:10.1109/TGRS.2006.888854, 2007. 6071

Tyynelä, J., and Chandrasekar, V.: Characterizing falling snow using multifrequency dual-polarization measurements, J. Geophys. Res.-Atmos., 119, 8268–8283, doi:10.1002/2013JD021369, 2014. 6065

TCD
9, 6061–6123, 2015

Vallese, F. and Kong, J. A.: Correlation function studies for snow and ice, J. Appl. Phys., 52, 4921 –4925, doi:10.1063/1.329453, 1981. 6063

Warren, S. G. and Brandt, R. E.: Optical constants of ice from the ultraviolet to the microwave: a revised compilation, J. Geophys. Res.-Atmos., 113, 1–10, doi:10.1029/2007JD009744, 2008. 6068

Werner, C., Wiesmann, A., Strozzi, T., Schneebeli, M., and Mätzler, C.: The SnowScat ground-based polarimetric scatterometer: Calibration and initial measurements from Davos Switzerland, in: Geoscience and Remote Sensing Symposium (IGARSS), 2010, IEEE International, 2363–2366, doi:10.1109/IGARSS.2010.5649015, 2010. 6065, 6078

West, R., Tsang, L., and Winebrenner, D. P.: Dense medium radiative transfer theory for two scattering layers with a Rayleigh distribution of particle sizes, IEEE T. Geosci. Remote, 31, 426–437, 1993. 6071

Wiesmann, A. and Mätzler, C.: Microwave emission model of layered snowpacks, Remote Sens. Environ., 70, 307–316, doi:10.1016/S0034-4257(99)00046-2, 1999. 6068, 6104

Wiesmann, A., Werner, C., Mätzler, C., Schneebeli, M., Strozzi, T., and Wegmuller, U.: Mobile X- to Ku-band scatterometer in support of the CoRe-H20 mission, in: Geoscience and Remote Sensing Symposium, 2008, IGARSS 2008, IEEE International, 5, V-244–V-247, doi:10.1109/IGARSS.2008.4780073, 2008. 6065, 6078

Xie, X., Löhnert, U., Kneifel, S., and Crewell, S.: Snow particle orientation observed by ground-based microwave radiometry, J. Geophys. Res.-Atmos., 117, 1–12, doi:10.1029/2011JD016369, 2012. 6065

TCD
9, 6061–6123, 2015

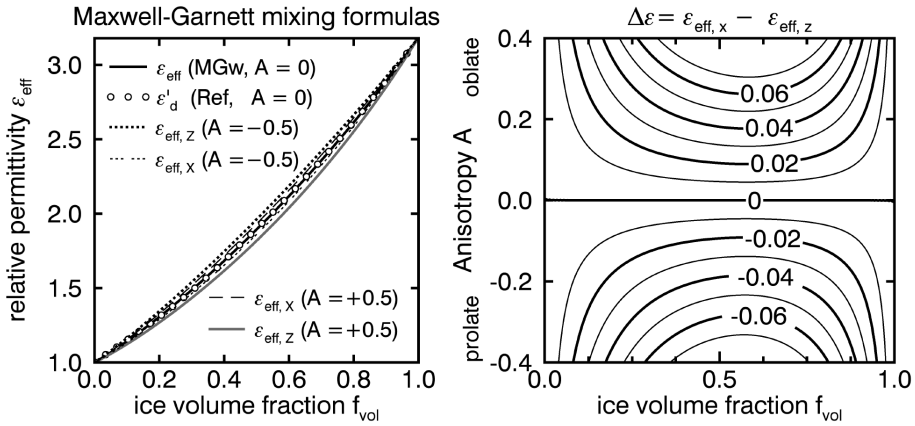

Figure 1. Left: Relative permittivity ε_{eff} of snow with isotropic ($A = 0$), vertically oriented ($A = -0.5$) and horizontally oriented ($A = +0.5$) inclusions calculated by the weighted Maxwell–Garnett formula (MGw), Eq. (3). The dots indicate the empirical function given by Eq. (46) in Wiesmann and Mätzler (1999). Right: the dielectric anisotropy, $\Delta\varepsilon = \varepsilon_{eff,x} - \varepsilon_{eff,z}$, as a function of ice volume fraction f_{vol} and anisotropy A according to Eq. (3).

TCD
9, 6061–6123, 2015

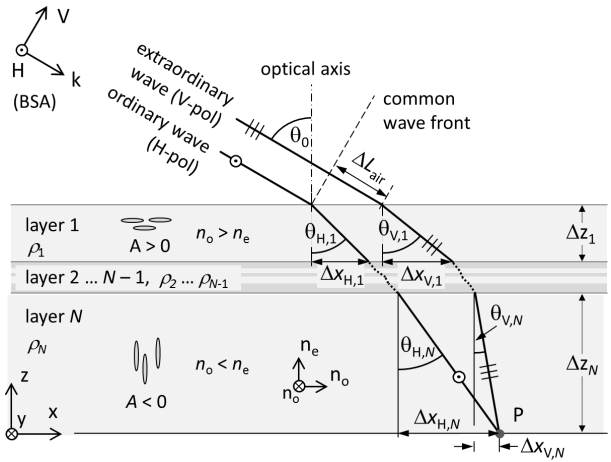

Figure 2. An electromagnetic wave (H or V polarized) is transmitted in ***k*** direction with respect to the radar coordinate system (H, k, V) and with an incidence angle θ_0 with respect to the snow surface. The electric field of the H polarized wave is perpendicular to the optical axis (z), and sees the ordinary refractive index n_o (therefore called the "ordinary wave"). The electric field of the V polarized wave has a component parallel to the optical axis and is affected by the extraordinary refractive index n_e (the "extraordinary wave"). For horizontally aligned anisotropies ($A > 0$) the extraordinary wave travels faster ($n_e < n_o$) whereas for vertical anisotropies the ordinary wave is faster ($n_o < n_e$). As refraction differs for both waves, also the optical distances differ when measured from a common wave front to the same point P on the ground. The anisotropy of the layers is shown as expected for fresh snow (layer 1) deposited on top of old snow (layer N). The layer of fresh snow with density ρ_1 and thickness Δz_1 is drawn with horizontal structures with a anisotropy $A > 0$. The thick layer of old snow is drawn as vertical ice grains ($A < 0$) recrystallized under temperature gradient metamorphism. The theory in this paper is true for any random layering of densities and anisotropies due to Snell's law as long as absorption or volume scattering are negligible.

TCD
9, 6061–6123, 2015

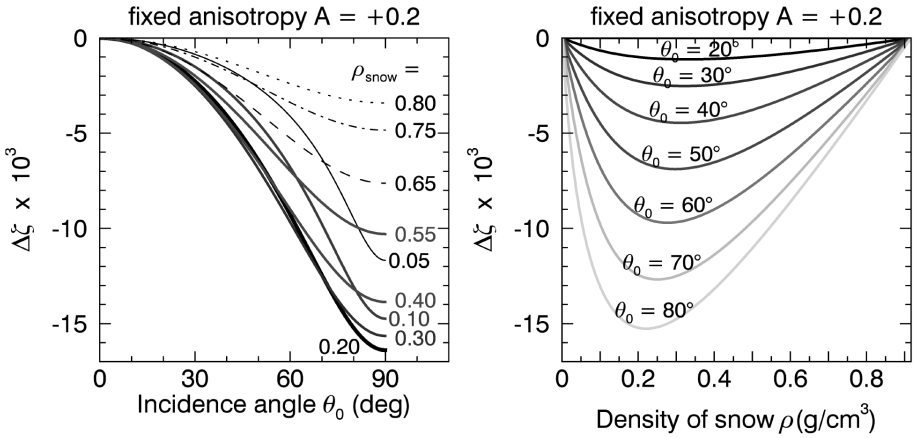

Figure 3. The relative path length difference $\Delta\zeta$, expected between vertically and horizontally polarized microwaves according to (Eq. 20), is plotted for snow with horizontally aligned oblate ice grains (A = +0.2) over incidence angle (left), and snow density (right).

TCD
9, 6061–6123, 2015

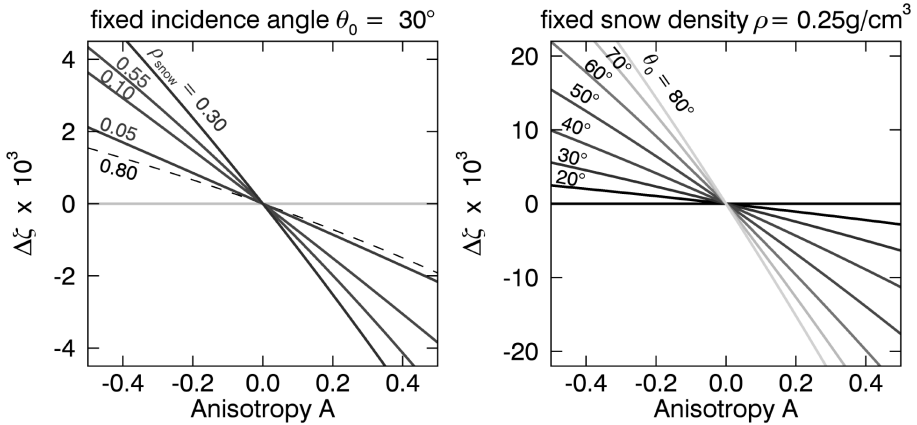

Figure 4. The relative path length difference $\Delta\zeta$, according to (Eq. 20), plotted over anisotropy for different snow densities but fixed incidence angle, $\theta_0 = 30^\circ$, (left) and for different incidence angles but fixed snow density, $\rho = 0.25\,\mathrm{g\,cm^{-3}}$, (right).

TCD
9, 6061–6123, 2015

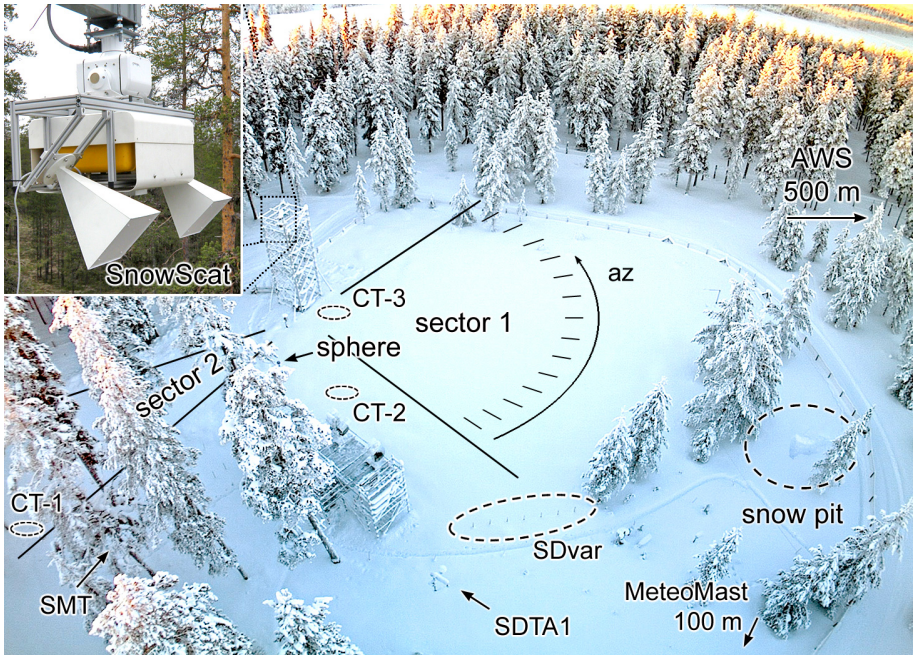

Figure 5. The radar data and meteorological measurements were acquired at the shown test site near the town of Sodankylä, Finland. The SnowScat Instrument, SSI, is shown in the inset and was mounted on a 9 m high tower. The reference target (sphere) used for calibration can be located behind a tree. The SSI scanned sector 1 and 2 with different azimuth and incidence angles. Meteorological sensors are named as follows: SDTA1: Snow depth and air temperature; SMT: Soil moisture and soil temperature; AWS: Automatic weather station. CT-1, CT-2 and CT-3 are the locations of snow profiles which were analyzed by computer tomography. Snow density was measured in the snow pit and was also derived from SWE determined by the SSI as described in (Leinss et al., 2015). The variability of snow depth was measured with seven sticks (SDvar).

TCD
9, 6061–6123, 2015

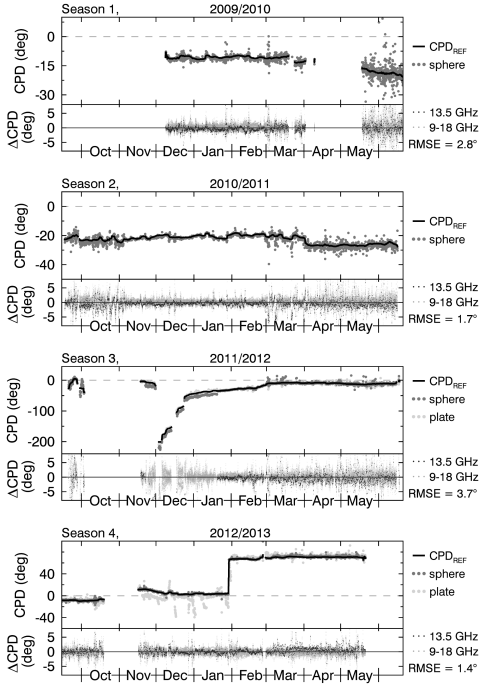

Figure 6. The CPD was calibrated using the sphere as a reference target. The upper panels show the reference, $CPD_{REF}(f)$, for f = 13.5 GHz (solid line) together with individual CPD measurements for the sphere and the plate (light and dark gray dots). The CPD of the metallic plate agrees within the standard deviation with measurements of the sphere and with CPD_{REF}. Deviations were found for season 3 due to a misalignment of the SSI to the sphere, and for November 2012, possibly due to snow cover of the metallic plate. The lower panels show the deviation, $\Delta CPD = CPD_{meas.}(f) - CPD_{REF}(f)$, for individual measurements at all measured frequencies f = 10–17 GHz. The deviation at a frequency of 13.5 GHz is shown as black dots. The standard deviation (RMSE) of ΔCPD for the whole frequency spectrum is given below the legend of the lower panel.

TCD
9, 6061–6123, 2015

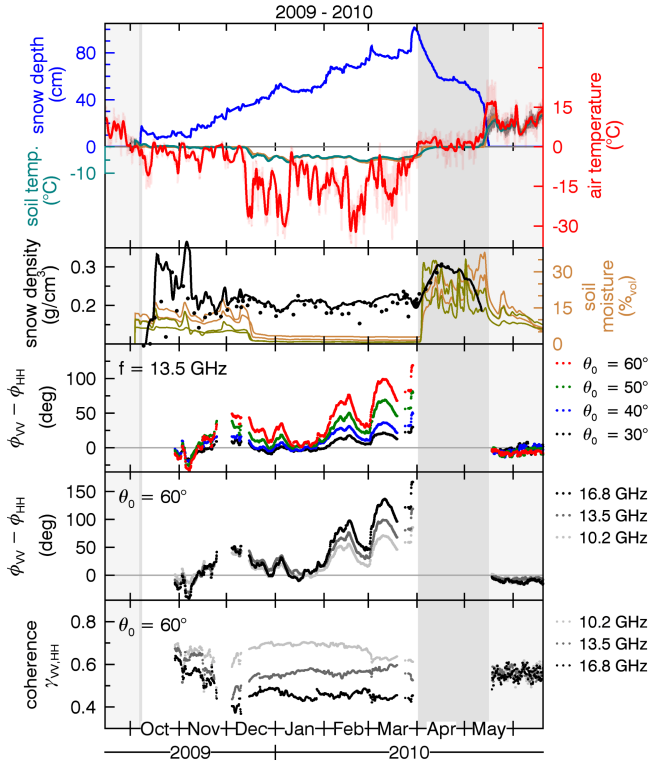

Figure 7. Winter season 2009–2010. Top three panels: Meteorological data measured by the sensors SDAT1 and SMT; snow density as described in Sect. 4.1. Bottom: CPD and copolar coherence measured by the SSI for different incidence angles and frequencies.

TCD
9, 6061–6123, 2015

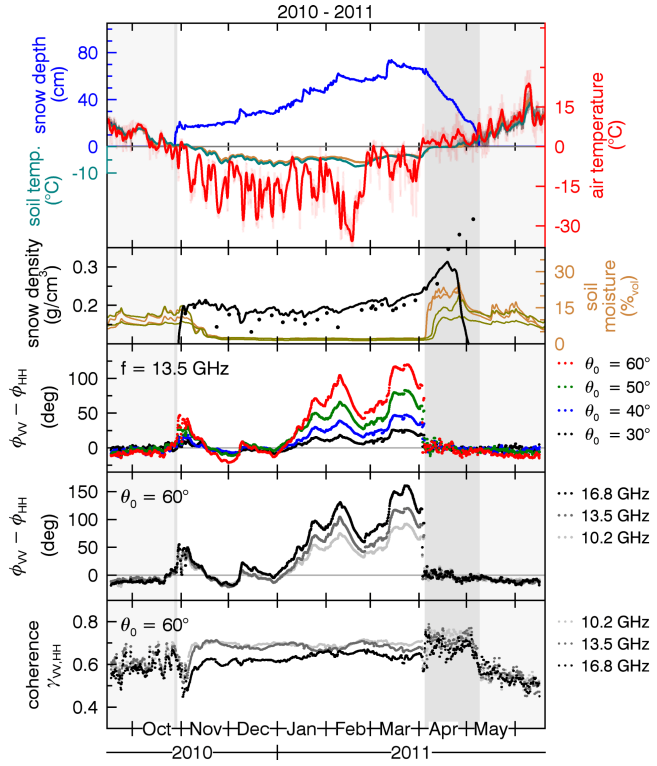

Figure 8. Winter season 2010–2011. Meteorological and radar data as shown in Fig. 7 and described in Sect. 4.1.

TCD
9, 6061–6123, 2015

Anisotropy of the snow pack measured by polarimetric phase differences

S. Leinss et al.

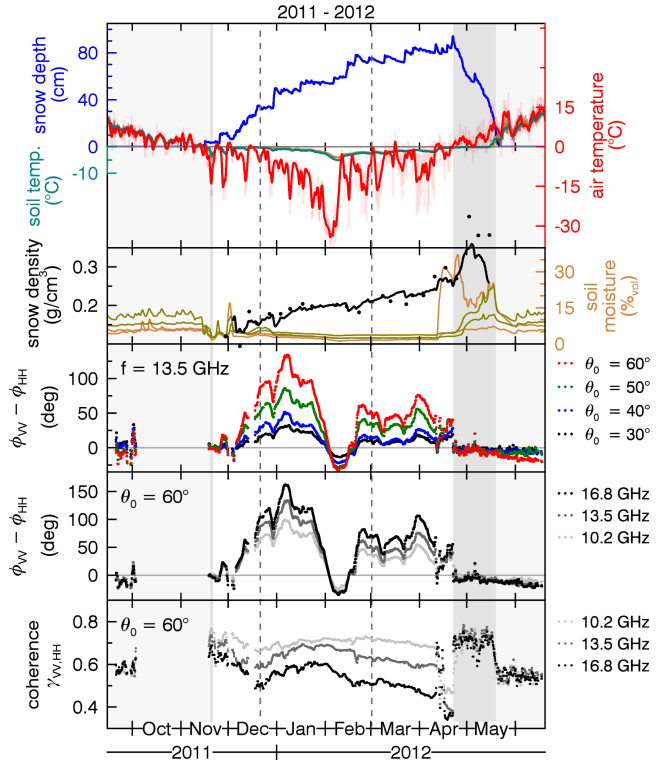

Figure 9. Winter season 2011–2012. Meteorological and radar data as shown in Fig. 7 and described in Sect. 4.1.

TCD
9, 6061–6123, 2015

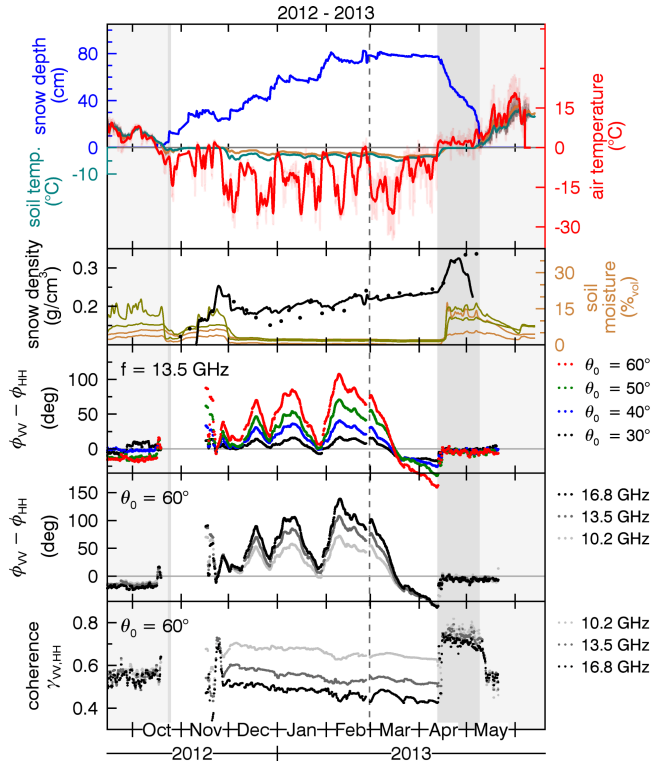

Figure 10. Winter season 2012–2013. Meteorological and radar data as shown in Fig. 7 and described in Sect. 4.1.

TCD
9, 6061–6123, 2015

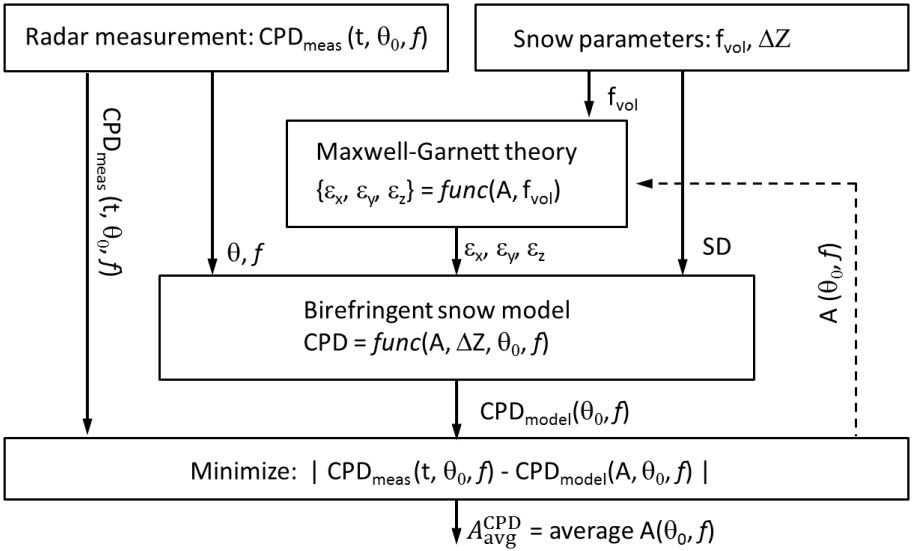

Figure 11. Processing chain used to estimate the average anisotropy of the snow pack, A_{avg}^{CPD}. The anisotropy can iteratively be estimated from the measured CPD, if snow depth ΔZ and the ice volume fraction f_{vol} are known. The anisotropy A was calculated independently for all incidence angles, θ_0, and frequencies, f, and the results were averaged.

TCD
9, 6061–6123, 2015

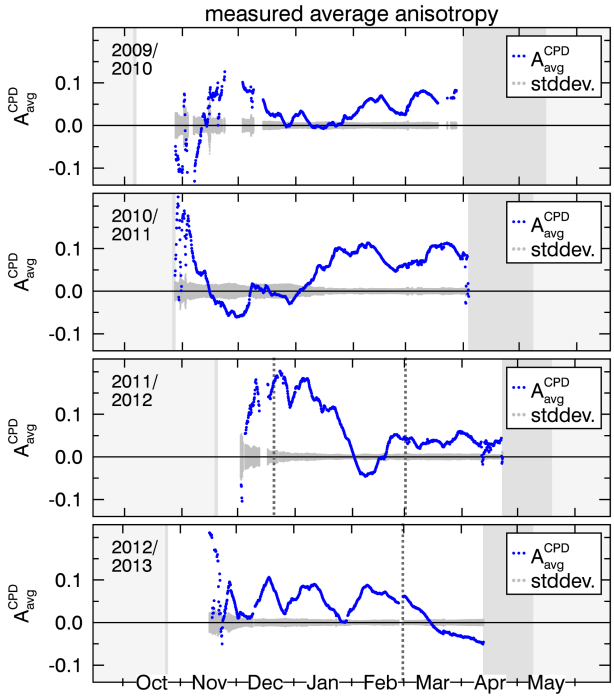

Figure 12. Average anisotropy of the snow pack, A^{CPD}_{avg}, determined during dry snow conditions for the winter seasons from 2009–2013. The anisotropy was derived from the CPD which was measured by the SnowScat instrument. The standard deviation of A^{CPD}_{avg}, calculated from measurements at different frequencies and incidence angles, is shown as the time-varying gray bar below the anisotropy. The dark-gray shading in April/May indicates the period of snow melt, the light-gray shadings in Oct./Nov. and May/June indicate snow free conditions. The dashed vertical lines show the times when the anisotropy was measured by computer tomography (CT-1, CT-2, CT-3).

TCD
9, 6061–6123, 2015

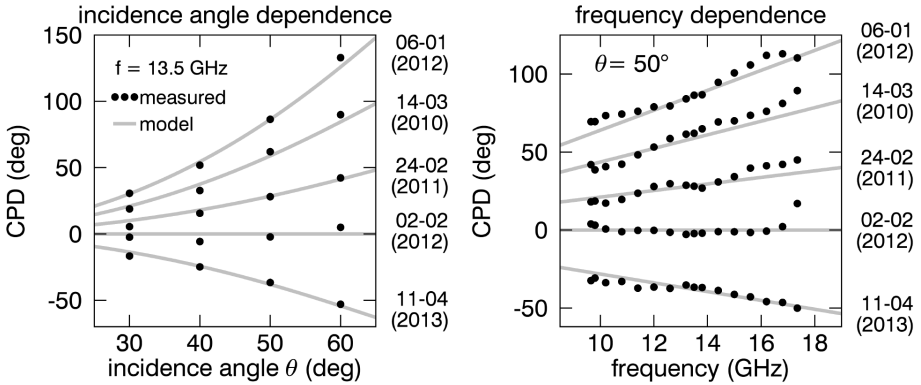

Figure 13. Left: incidence angle dependence of measured CPD vs. modeled incidence angle dependence. Right: frequency dependence of measured CPD vs. modeled linear frequency dependence.

TCD
9, 6061–6123, 2015

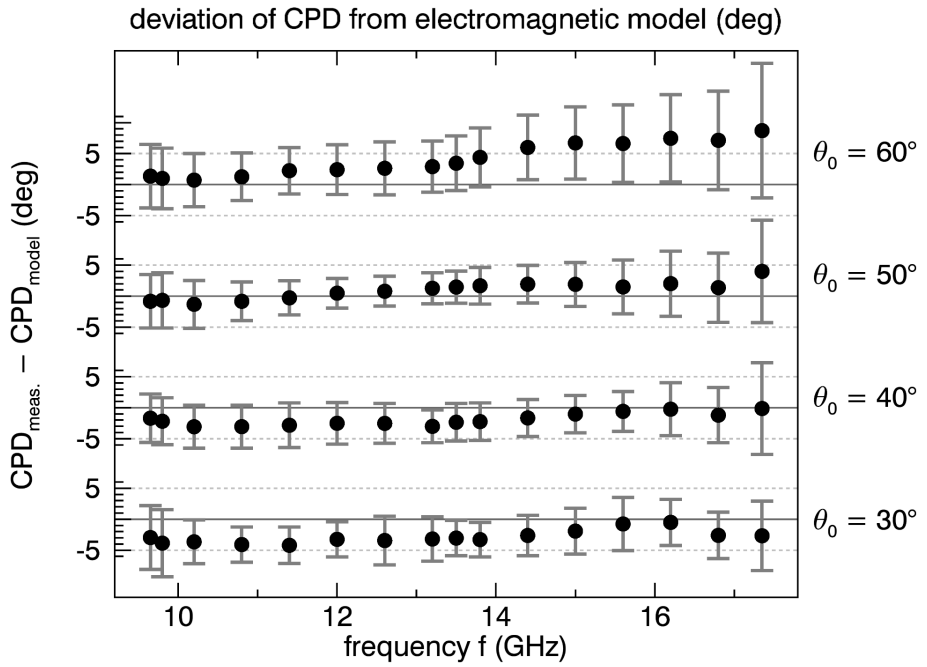

Figure 14. Deviation of measured and modeled CPD for different frequencies f and different incidence angles θ_0. Dots show the mean deviation $CPD_{meas.} - CPD_{modeled}$ of all data acquired during dry snow conditions. The error bars are the standard-deviations calculated from about 5600 measurements.

TCD
9, 6061–6123, 2015

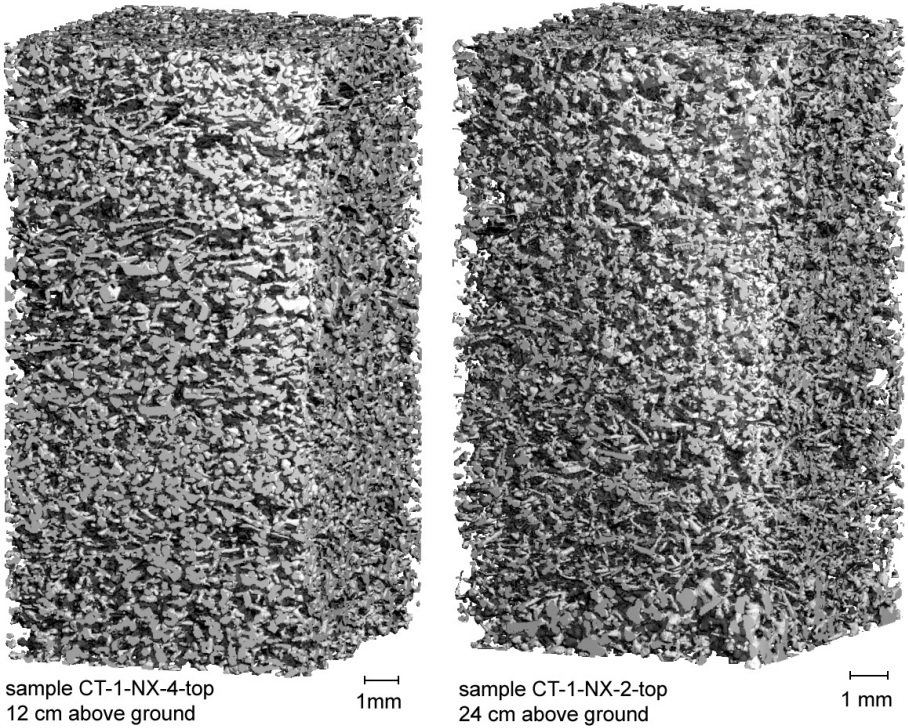

Figure 15. Two samples from the profile CT-1 (21 December 2011) taken at a depth of 12 cm (left) and 24 cm (right) above ground. Horizontal structures can be identified in both images. The average anisotropy derived for the two samples are $A_{\mathrm{avg}}^{\mathrm{CT}} = +0.26$ (left) and +0.16 (right). The vertically resolved anisotropy, A_{CT}, determined every 2 mm depth by means of μCT, are plotted in Fig. 17 (top left) for both samples as blue dots.

TCD
9, 6061–6123, 2015

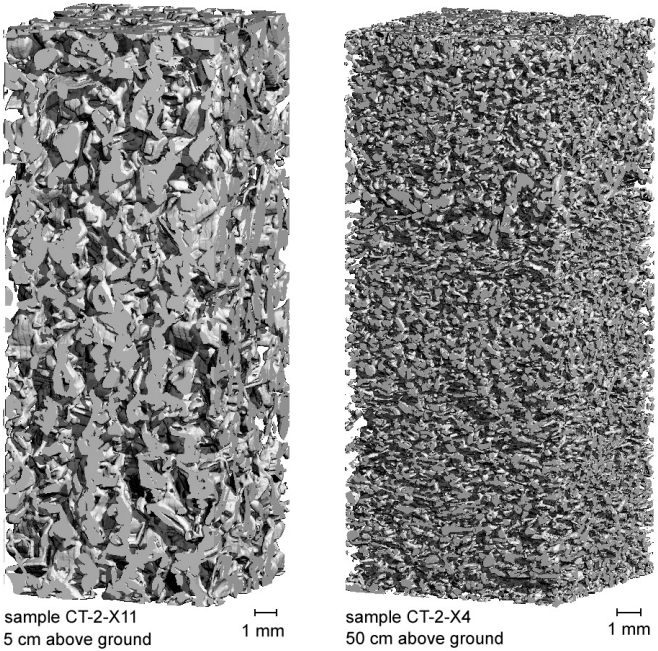

Figure 16. Two samples from the profile CT-2 (1 March 2012). The left profile, taken 5 cm above ground, shows old recrystallized snow (depth hoar) with vertical structures ($A^{CT}_{avg} = -0.24$). The profile on the right, taken 50 cm above ground, shows horizontal structures ($A^{CT}_{avg} = +0.35$) of fresh, settled snow which fell two weeks before the sample was taken. The vertically resolved anisotropy, A_{CT}, determined every 2–5 mm depth by means of μCT, are plotted in Fig. 17 (top right) for both samples as blue dots.

TCD
9, 6061–6123, 2015

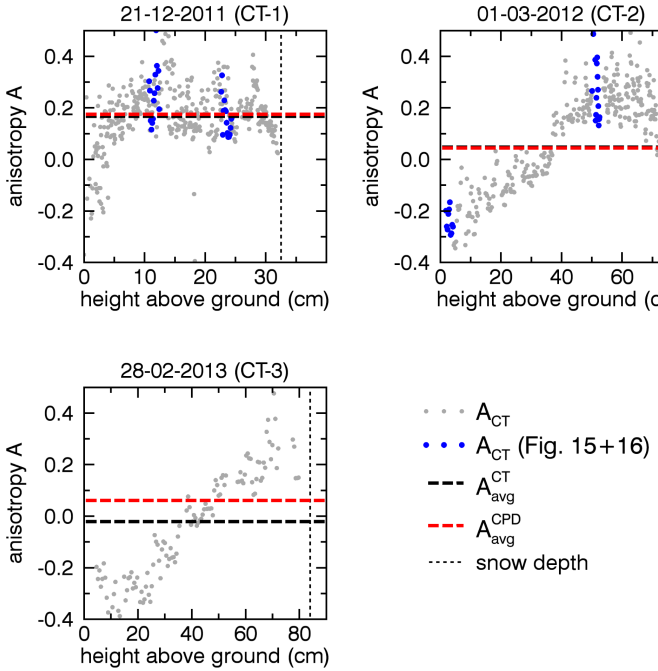

Figure 17. Vertical profiles of the anisotropy, A_{CT}, determined from computer tomography. For comparison, we plotted in each graph horizontal lines which show the depth-averaged anisotropies, A_{avg}^{CT} together with the average anisotropy, A_{avg}^{CPD}, determined from the radar data (Fig. 12). Top-left: the profile CT-1 shows homogeneously distributed positive anisotropies which result from heavy snow fall during mild temperatures in December 2011 (Fig. 9). Top-right: The profile CT-2 shows a thick layer with vertical structures of recrystallized snow in the lower 35 cm of the snow pack. In the upper 35 cm horizontal structures are visible which result from fresh snow fall mid of February 2012 (see Fig. 9). Bottom-left: alternating snow fall and cold temperatures lead to an almost linearly increasing anisotropy in the end of February 2013 (see Fig. 10).

TCD
9, 6061–6123, 2015

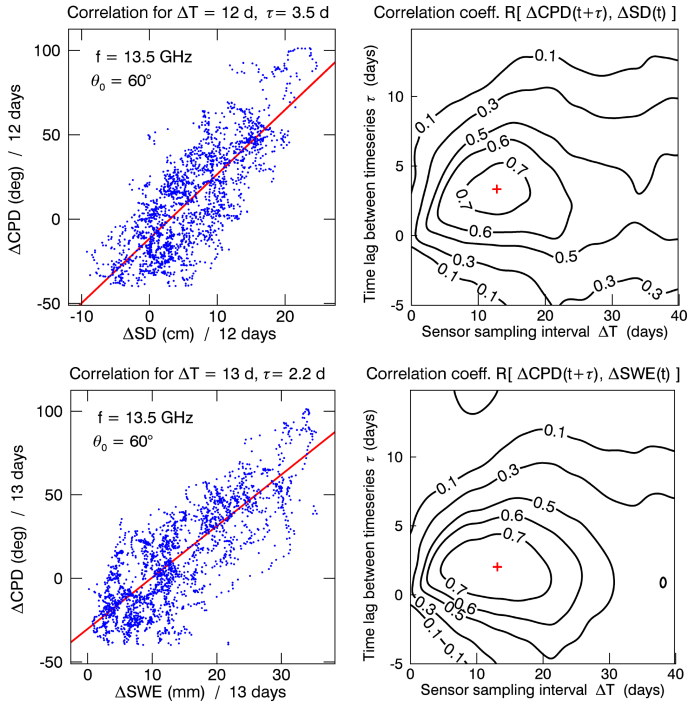

Figure 18. Left: correlation between ΔCPD and changes in snow depth ΔSD (top) and ΔSWE (bottom) within a sampling interval of ΔT = 12 and 13 days. The time when the CPD difference was obtained, $t + \tau$, was shifted by τ = 3.5 days (top) and τ = 2.2 days (bottom) vs. the time t when the snow depth difference ΔSD was obtained because the maximum CPD was always observed when fresh snow has already settled. Right: Pearson-correlation coefficients R for different pairs of ΔT and τ shown as contour plots. The pair $(\Delta T, \tau)$ with the highest correlation coefficient is marked by a red cross.

TCD
9, 6061–6123, 2015

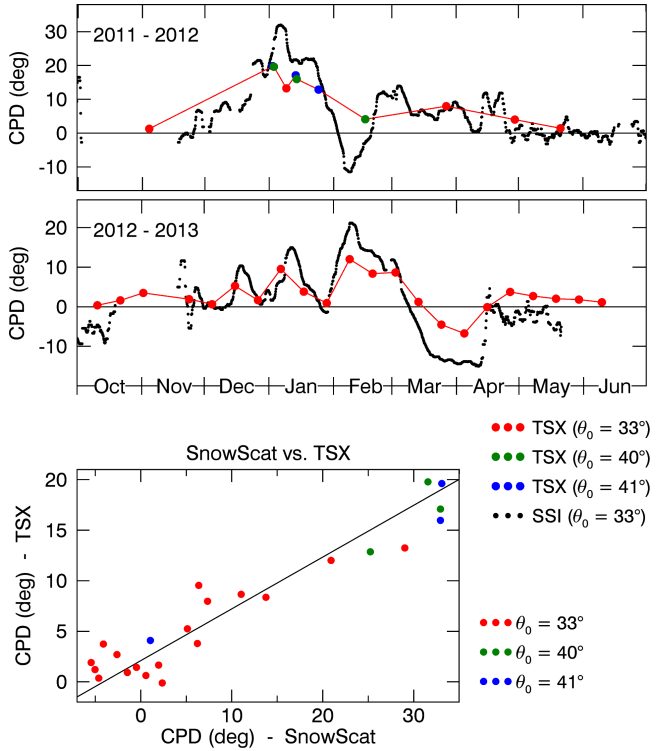

Figure 19. CPD measured by TerraSAR-X at θ = 33, 40, and 41° in comparison with measurements of the SnowScat instrument (f = 9.65 GHz, interpolated to θ = 33°). The measurements of both instruments show the same trend but the CPD measurements of the SSI are about a factor of 2 larger than the TSX measurements. The discrepancy can be explained by different snow conditions as the TSX data were acquired over open areas, where about 30 % less snow depth was measured, compared to the test site of the SSI.

TCD
9, 6061–6123, 2015

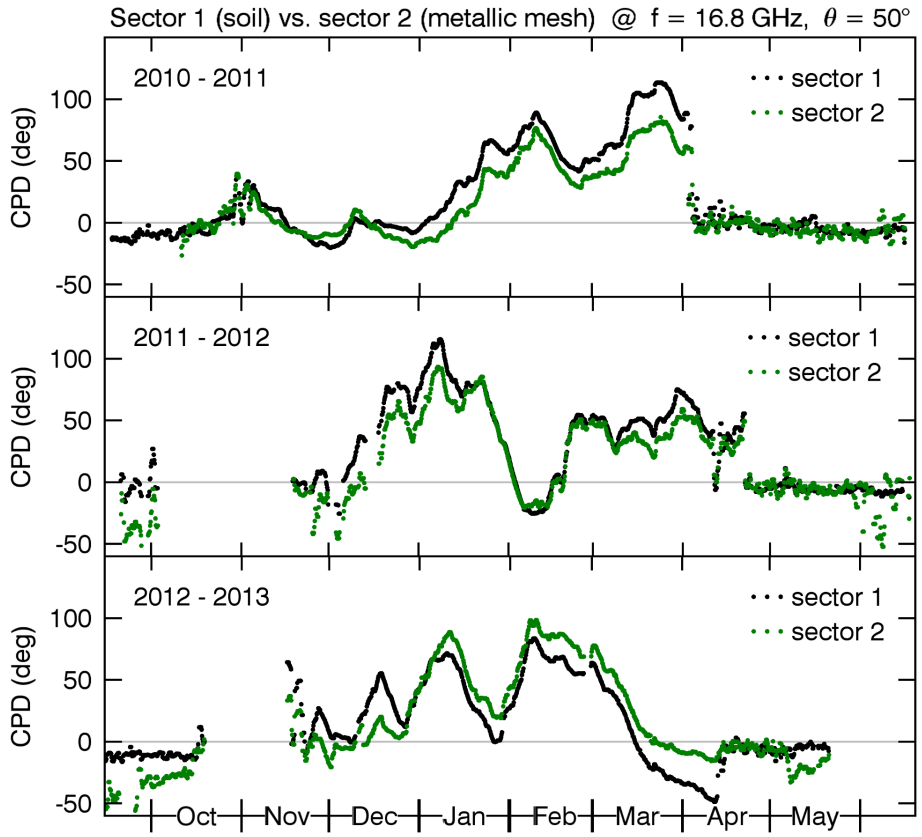

Figure 20. Comparison of the CPD measured on the two sectors of the test site. Sector 2 was located between trees behind the SnowScat instrument, and was covered with a metallic mesh during the last two seasons of the experiment (after August 2011). Generally, the CPD on sector 2 evolves very similar to Sector 1 and does not show large deviations.

TCD
9, 6061–6123, 2015